Permeability effects on the seismic response of gas reservoirs

J. Germán Rubino,[1] Danilo R. Velis[2] and Klaus Holliger[1]

[1]*Institute of Geophysics, University of Lausanne,* CH-1015 *Lausanne, Switzerland. E-mail: german.rubino@unil.ch*
[2]*Facultad de Ciencias Astronómicas y Geofísicas, Universidad Nacional de La Plata, and CONICET, Argentina*

SUMMARY

In this work, we analyse the role of permeability on the seismic response of sandstone reservoirs characterized by patchy gas–water saturation. We do this in the framework of Johnson's model, which is a generalization of White's seminal model allowing for patches of arbitrary geometry. We first assess the seismic attenuation and velocity dispersion characteristics in response to wave-induced fluid flow. To this end, we perform an exhaustive analysis of the sensitivity of attenuation and velocity dispersion of compressional body waves to permeability and explore the roles played by the Johnson parameters T and S/V, which characterize the shape and size of the gas–water patches. Our results indicate that, within the typical frequency range of exploration seismic data, this sensitivity may indeed be particularly strong for a variety of realistic and relevant scenarios. Next, we extend our analysis to the corresponding effects on surface-based reflection seismic data for two pertinent models of typical sandstone reservoirs. In the case of softer and more porous formations and in the presence of relatively low levels of gas saturation we observe that the effects of permeability on seismic reflection data are indeed significant. These prominent permeability effects prevail for normal-incidence and non-normal-incidence seismic data and for a very wide range of sizes and shapes of the gas–water patches. For harder and less porous reservoirs, the normal-incidence seismic responses exhibit little or no sensitivity to permeability, but the corresponding non-normal-incidence responses show a clear dependence on this parameter, again especially so for low gas saturations. The results of this study therefore suggest that, for a range of fairly common and realistic conditions, surface-based seismic reflection data are indeed remarkably sensitive to the permeability of gas reservoirs and thus have the potential of providing corresponding first-order constraints.

Key words: Permeability and porosity; Seismic attenuation; Computational seismology; Wave propagation; Acoustic properties.

1 INTRODUCTION

Permeability is a measure of the capacity for fluid movement in porous or fractured media. As such it is arguably the most important, but also the most elusive, hydraulic parameter as, commonly, it can only be measured through dedicated laboratory and field experiments (e.g. Butler 2005). Geophysical constraints with regard to the spatial distribution of subsurface hydraulic parameters are considered to be especially valuable as the corresponding methods are comparatively cheap and non-invasive and, quite importantly, because they have the potential to bridge the inherent gap in terms of spatial resolution and coverage that exists between traditional techniques, such as core analyses and tracer or pumping tests (e.g. Hubbard & Rubin 2005). Although standard geophysical techniques cannot in general provide any direct information on the permeability of the probed medium, there are some more specialized approaches that exhibit a more or less direct sensitivity to this important parameter. Together with nuclear magnetic resonance measurements (e.g.

Ellis & Singer 2008), analyses of seismic observations arguably represent the most promising avenues to this end (e.g. Pride *et al.* 2003).

The methodological foundations of seismic wave propagation in porous media are generally credited to Biot (1956a,b). The corresponding theoretical framework is now commonly referred to as poroelasticity (e.g. Carcione 2007) and establishes critical links between the seismic and hydraulic properties of saturated porous media and thus holds the promise of deriving permeability estimates from seismic observations (e.g. Pride *et al.* 2003; Pride 2005). In its classical form, Biot theory assumes that wave-induced fluid movements at the macroscopic scale, as defined by the predominant wavelengths, are the cause of seismic attenuation and velocity dispersion. To date, probably some of the most tangible results of corresponding research efforts in the poroelastic interpretation of seismic data are borehole-based permeability estimates obtained from the analysis of Stoneley waves (e.g. Tang & Cheng 1996, 2004).

Conversely, only scarce and inconclusive evidence is available with regard to the possibility of obtaining permeability constraints from a poroelastic interpretation of surface-based seismic data (e.g. De Barros & Dietrich 2008; De Barros *et al*. 2010). A likely reason for this is that classical Biot theory dramatically underestimates the attenuation of seismic waves in the frequency range typical of exploration seismic data (e.g. Pride *et al*. 2004).

Additional loss mechanisms were therefore proposed to explain the high levels of attenuation observed in seismic data. The so-called local fluid flow or squirt flow loss mechanism (e.g. Dvorkin *et al*. 1995) is associated with wave-induced fluid flow at microscopic scales. That is, when a seismic wave compresses a rock containing grain-scale damage zones, such as microcracks or broken grain contacts, it induces a fluid pressure gradient between the pore fluid lying in the main pore space and that located in the cracks. This, in turn, produces fluid flow from cracks to the main pore space and, consequently, seismic attenuation and velocity dispersion. Although this loss mechanism may play an important role in the sonic and ultrasonic range of frequencies, it does not seem to be able to explain the high levels of attenuation typically observed at seismic frequencies (Pride *et al*. 2004).

Another complementary loss mechanism is related to the presence of mesoscopic heterogeneities, that is, heterogeneities that are larger than the pore size but smaller than the prevailing seismic wavelengths (White 1975; White *et al*. 1975). Due to the different physical properties of the mesoscale regions composing a heterogeneous medium, seismic waves generate fluid flow between them, which in turn manifests itself in the form of attenuation and velocity dispersion effects. This loss mechanism strongly depends on the rock frame properties as well as on the nature and composition of the pore fluids. Moreover, this attenuation mechanism critically depends on the permeability, since it is governed by fluid pressure equilibration occurring between the different regions of the probed heterogeneous rock volume. Together with the fact that there is increasing evidence indicating that this physical process constitutes the dominant seismic attenuation mechanism in reservoir rocks in the frequency range typical of exploration-type data (e.g. Pride *et al*. 2003, 2004; Carcione & Picotti 2006), this lead some researchers to study the role of permeability on seismic data in the framework of mesoscopic effects. Notably, Pride *et al*. (2003) explored the question of whether seismic data contain information about permeability. They concluded that seismic amplitudes might contain this kind of information, and thus, in principle, permeability estimates could be derived from three-component seismic data using full-waveform inversion procedures based on the Biot's equations and accounting for the presence of mesoscopic heterogeneities. It goes without saying that knowledge of the sensitivity kernels for wave propagation in porous media (e.g. Morency *et al*. 2009) would be essential tools for the development of such inversion procedures. The main practical problem is that extremely fine meshes would be needed to adequately represent the mesoscopic heterogeneities and to properly solve the wave-induced fluid pressure equilibration processes taking place between the different regions of the medium. Moreover, the problem of separating the relative contributions of poroelastic and non-poroelastic effects to the total observed attenuation is still largely unresolved. The actual inverse problem is therefore outside the scope of this paper and the reader is referred to the work of Pride *et al*. (2003) for a lucid, in-depth discussion of this topic.

Recently, Kozlov (2007) studied permeability effects on the seismic response of a permeable layer defined by a dual-porosity model that takes into account interconnected fractures and intergranular pores. His findings indicate that the seismic response of reservoir layers indeed carries permeability information in their frequency spectra. Ren *et al*. (2009) came to similar conclusions when analysing the role of permeability in the case of porous media consisting of a stack of thin layers alternately saturated with gas and water (White *et al*. 1975). Goloshubin *et al*. (2008) used fluid flow and scattering mechanisms to obtain a frequency-dependent seismic attribute, which in turn led them to estimate reservoir permeability.

It is important to mention here that, as shown by Shapiro & Müller (1999), in the case of heterogeneous porous media having strong permeability fluctuations, there is a discrepancy between effective flow permeability and the permeability controlling seismic attenuation due to wave-induced fluid flow. These authors modelled attenuation in randomly layered poroelastic media with strong permeability fluctuations and observed that the arithmetic average over the layer permeabilities produced better estimates of the mesoscopic attenuation than the corresponding curves obtained using the effective vertical flow permeability given by the harmonic average. Later, Müller *et al*. (2007) showed that the frequency dependence of the effective permeability has to be taken into account to properly model seismic attenuation due to wave-induced fluid flow in these kinds of media.

In the context of wave-induced fluid flow effects, the case of patchy gas–water saturation, that is, gas–water distributions in the form of patches fully saturated with gas embedded in regions fully saturated with water, is particularly interesting. The reason for this is that mesoscopic heterogeneities of this kind may produce particularly strong attenuation and velocity dispersion effects (e.g. White 1975; White *et al*. 1975) due to the very high compressibility of gas as compared with that of water. Rubino *et al*. (2011) showed that, for certain CO_2 saturation values and patch geometries, the corresponding effects on surface-based seismic reflection data can be very significant. Indeed, the available evidence indicates that the corresponding attenuation and velocity dispersion effects are likely to prevail over those related to other potential loss mechanisms (e.g. Pride *et al*. 2003, 2004). For these reasons, porous media characterized by patchy gas–water saturations seem to be particularly suitable for studying the influence of permeability on seismic data in the framework of mesoscopic effects. To our knowledge, the potential of obtaining constraints on permeability from surface-based seismic reflection data is, however, largely unexplored. A recent effort in this direction was presented by Ren *et al*. (2009), who studied the dependence of the normal-incidence reflection coefficient on permeability for gas reservoirs. Their analysis included both a low- and a high-impedance reservoir model composed of stacks of 1-m-thick layers alternately saturated with gas and water (White *et al*. 1975). The gas saturation and patch geometry were thus constant and uniform and hence did not allow for any generic insights into the sensitivity of surface-based seismic reflection data with regard to permeability.

In this paper, we address this problem by studying the role of permeability in homogeneous sandstone reservoirs characterized by patchy gas–water saturation on seismic attenuation and velocity dispersion in general and on surface-based seismic reflection data in particular. Specifically, we seek to establish under which conditions seismic reflection data can be expected to be sensitive to permeability. Using the theory of Johnson (2001) and considering a variety of geometries and sizes for the gas patches as well as a wide range of saturation and permeability values, we first explore body wave attenuation and velocity dispersion effects for a soft and porous sandstone reservoir as well as for a harder and less porous equivalent. Next, we explore the behaviour of compressional and shear

waves reflected from the top of the gas reservoirs as a function of permeability for both normal-incidence and non-normal-incidence seismic reflection data. Finally, we perform numerical simulations of surface-based seismic reflection data to assess the attenuation and velocity dispersion effects on the recorded traces for a wide range of permeability values.

2 SEISMIC ATTENUATION AND VELOCITY DISPERSION DUE TO PATCHY SATURATION

2.1 Methodological background

White and coauthors (White 1975; White *et al.* 1975) were the first to propose the presence of patchy gas–water distributions as an important cause of seismic energy loss. To this end, they analysed the seismic response of a stack of porous layers alternately saturated with gas and water (White *et al.* 1975) as well as of spherical gas patches in an otherwise water-saturated rock matrix (White 1975). Subsequently, a large number of authors have made significant contributions to explore this topic in more detail (e.g. Dutta & Odé 1979; Johnson 2001; Müller & Gurevich 2005; Masson & Pride 2011).

When a compressional wave travels across a medium characterized by patchy saturation it will induce very different pore pressures for the two fluids due to the distinct physical properties of gas and water. The corresponding pore pressure equilibration process is then governed by Biot's (1956b) diffusive slow wave, the diffusion length of which is given by

$$L_{\mathrm{d}} = \sqrt{D/\omega}, \tag{1}$$

where ω is the angular frequency and D is the diffusivity defined as (e.g. Pride 2005)

$$D = \frac{\kappa}{\eta} \left(\frac{M_{\mathrm{c}} K_{\mathrm{av}} - \alpha^2 K_{\mathrm{av}}^2}{M_{\mathrm{c}}} \right). \tag{2}$$

Here, κ and η denote the permeability of the rock and the fluid viscosity, respectively. In addition, the parameters M_{c}, K_{av} and α can be expressed in terms of the physical properties of the fluid-saturated porous media (e.g. Rubino *et al.* 2009):

$$\alpha = 1 - \frac{K_{\mathrm{m}}}{K_{\mathrm{s}}}, \tag{3}$$

$$K_{\mathrm{av}}(K_{\mathrm{f}}) = \left(\frac{\alpha - \phi}{K_{\mathrm{s}}} + \frac{\phi}{K_{\mathrm{f}}} \right)^{-1}, \tag{4}$$

and

$$M_{\mathrm{c}}(K_{\mathrm{f}}) = K_{\mathrm{G}}(K_{\mathrm{f}}) + \frac{4}{3}\mu, \tag{5}$$

where

$$K_{\mathrm{G}}(K_{\mathrm{f}}) = K_{\mathrm{m}} + \alpha^2 K_{\mathrm{av}}(K_{\mathrm{f}}). \tag{6}$$

In these expressions, K_{s}, K_{m}, and K_{f} are the bulk moduli of the solid grains, the dry matrix and the fluid phase, respectively, μ is the shear modulus of the fluid-saturated porous rock, which is assumed to be equal to the shear modulus of the dry frame, and ϕ is the porosity.

At sufficiently low frequencies, as characterized by diffusion lengths that are much larger than the patch sizes, there will be enough time during each half-cycle of oscillation for the pressure of the pore fluid to equilibrate at a common value (Johnson 2001). Under such conditions, the pore pressure is thus uniform and the

effective bulk modulus of the pore fluid is given by Wood's (1955) law

$$K_{\mathrm{R}} = \left(\frac{S_{\mathrm{g}}}{K_{\mathrm{g}}} + \frac{S_{\mathrm{w}}}{K_{\mathrm{w}}} \right)^{-1}, \tag{7}$$

where S_i and K_i are the saturation and the bulk modulus of the gas ($i = \mathrm{g}$) and water ($i = \mathrm{w}$), respectively. Therefore, regardless of the geometry of the gas patches, the effective bulk modulus of the rock sample at the low-frequency limit is real-valued and given by the so-called Gassmann expression (e.g. Mavko *et al.* 2009)

$$K_{\mathrm{GW}} = K_{\mathrm{G}}(K_{\mathrm{R}}) = K_{\mathrm{m}} + \alpha^2 K_{\mathrm{av}}(K_{\mathrm{R}}), \tag{8}$$

for a fictitious fluid with a bulk modulus K_{R} given by eq. (7) (Johnson 2001).

On the other hand, when the frequencies are very high, the diffusion lengths are very small compared to the patch sizes and there is no time for communication between the pore fluid of the different regions. In this case, the pore pressure is not uniform, but to a first approximation can be assumed to be constant within each pore fluid phase (Johnson 2001). The bulk moduli of the two regions are then given by the Gassmann expression, $K_{\mathrm{G}}(K_i)$ with $i = \mathrm{g}$, w (eq. 6). In addition, Hill's (1964) theorem gives the corresponding composite bulk modulus, K_{GH}, at the high-frequency limit, which is also real-valued and satisfies (Johnson 2001)

$$\frac{1}{K_{\mathrm{GH}} + (4/3)\mu} = \frac{S_{\mathrm{g}}}{K_{\mathrm{G}}(K_{\mathrm{g}}) + (4/3)\mu} + \frac{S_{\mathrm{w}}}{K_{\mathrm{G}}(K_{\mathrm{w}}) + (4/3)\mu}. \tag{9}$$

For intermediate frequencies, as characterized by diffusion lengths that are of similar size as the heterogeneities, significant fluid flow can be induced by the compressional wave, which in turn can generate significant attenuation and velocity dispersion effects. This attenuation mechanism exhibits a maximum in the vicinity of the frequency ω_0, at which the diffusion length L_{d} equals the characteristic length h of the heterogeneities (Gurevich & Lopatnikov 1995). From eqs (1), (2), (5) and (6), we thus obtain

$$\omega_0 = \frac{K_{\mathrm{av}}(K_{\mathrm{m}} + \frac{4}{3}\mu)}{M_{\mathrm{c}}\eta} \left(\frac{\kappa}{h^2} \right), \tag{10}$$

where the different parameters are computed in the region containing water (Picotti *et al.* 2010). This equation is particularly interesting, since it shows the strong influence of permeability on the position of the loss peak. Depending on the position of the loss peak with respect to the prevailing frequencies, this physical parameter may therefore affect significantly the seismic response of a given gas reservoir.

The dynamic bulk modulus $\tilde{K}(\omega)$, which is a complex-valued and frequency-dependent function, describes the crossover from K_{GW} in the low-frequency limit to K_{GH} in the high-frequency limit according to the geometrical characteristics of the gas patches. In this work, we follow Johnson's (2001) model to determine $\tilde{K}(\omega)$, which is a generalization of White's (1975) models for a homogeneous rock frame having fluid patches of arbitrary shape defined by only two geometrical parameters in addition to those inherent in conventional Biot (1956b) theory. To define the dynamic bulk modulus, Johnson (2001) assumes a simple expression that ensures causality of the solution

$$\tilde{K}(\omega) = K_{\mathrm{GH}} - \frac{K_{\mathrm{GH}} - K_{\mathrm{GW}}}{1 - \zeta + \zeta\sqrt{1 + \mathrm{j}\omega\tau/\zeta^2}}, \tag{11}$$

where $\mathrm{j} = \sqrt{-1}$ is the imaginary number, ζ and τ can be written in terms of the physical properties of the dry rock and fluid phases and the two 'geometrical' parameters S/V and T denoting the specific

Table 1. Material properties for the models considered in this study.

	Sandstone 1	Sandstone 2
Grain bulk modulus[a] (GPa)	$K_s = 37$	$K_s = 37$
Grain density[a] (g cm^{-3})	$\rho_s = 2.65$	$\rho_s = 2.65$
Dry rock bulk modulus (GPa)	$K_m = 4.8$	$K_m = 17.2$
Dry rock shear modulus (GPa)	$\mu = 5.7$	$\mu = 20.45$
Porosity	$\phi = 0.3$	$\phi = 0.15$

	Water	Gas
Density[a] (g cm^{-3})	$\rho_w = 1.04$	$\rho_g = 0.078$
Bulk modulus[a] (GPa)	$K_w = 2.25$	$K_g = 0.012$
Viscosity [a] (P)	$\eta_w = 0.03$	$\eta_g = 0.0015$

[a] Parameters adopted from Rubino *et al.* (2009).

surface area of the patches and a measure of the patch size of the stiff fluid, respectively (Johnson 2001). These parameters, which are now generally referred to as Johnson parameters, are described in more detail in Appendix A.

This complex-valued and frequency-dependent dynamic bulk modulus (eq. 11) then allows for obtaining the corresponding complex compressional velocity (e.g. Rubino *et al.* 2009)

$$V_{pc}(\omega) = \sqrt{\frac{\tilde{K}(\omega) + \frac{4}{3}\mu}{\rho_b}}, \tag{12}$$

where ρ_b is the bulk density given by

$$\rho_b = (1 - \phi)\rho_s + \phi(S_g\rho_g + S_w\rho_w). \tag{13}$$

Here, ρ_s, ρ_g and ρ_w denote the densities of the solid grains, gas, and water, respectively. The complex compressional velocity (eq. 12)

then lets us obtain the equivalent phase velocity $V_p(\omega)$ and inverse quality factor $1/Q(\omega)$ (e.g. Rubino *et al.* 2009)

$$V_p(\omega) = \left[\Re\left(\frac{1}{V_{pc}(\omega)}\right)\right]^{-1}, \tag{14}$$

$$\frac{1}{Q(\omega)} = \frac{\Im\left[V_{pc}(\omega)^2\right]}{\Re\left[V_{pc}(\omega)^2\right]}. \tag{15}$$

2.2 Numerical analysis

To illustrate the role of permeability on compressional seismic waves travelling through sandstone reservoirs characterized by patchy gas–water saturation, we consider different geometries and sizes of the patches and compute the corresponding attenuation and velocity dispersion curves using Johnson's (2001) model for a pertinent range of permeability values. We consider two kinds of sandstones for our reservoir models: a soft and highly porous formation, denoted as 'sandstone 1', and a harder, less porous formation, denoted as 'sandstone 2'. Table 1 shows the pertinent material properties for the two reservoirs as well as those for the pore fluids. Please note that the elastic moduli of the dry frames were computed from the porosity and the properties of the solid grains according to the model of Krief *et al.* (1990).

As a first approach to study these types of media, we consider spherical gas pockets similar to those proposed by White (1975) characterized by an inner zone of radius R_g fully saturated with gas surrounded by a water-filled zone of radius R_w. We employ Johnson's (2001) model to obtain the responses of the media under consideration and determine the parameters T and S/V according to the corresponding geometry (Appendix A). Fig. 1 shows, for
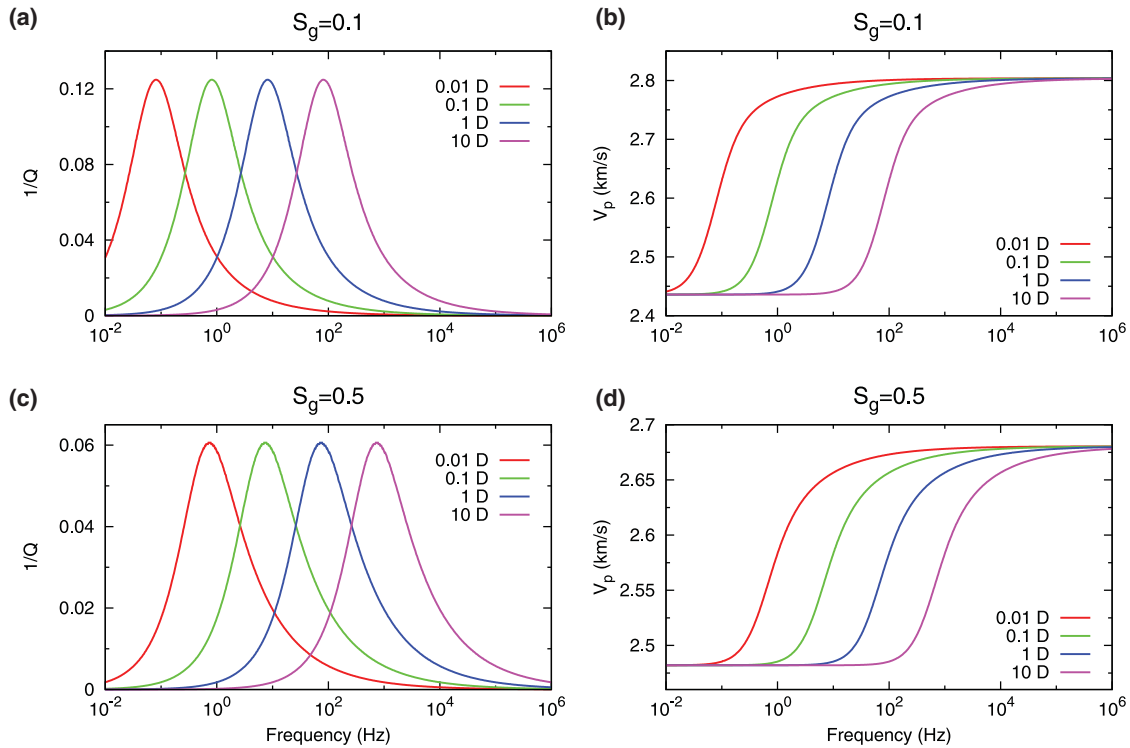

Figure 1. (a,c) Inverse quality factor and (b,d) phase velocity for the spherical White's (1975) model considering an outer radius $R_w = 0.4$ m and the sandstone 1 (Table 1). The different curves correspond to different permeability values, as indicated by the corresponding legend. Permeability is given in units of darcies (D) with 1 D $\simeq 0.987 \times 10^{-12}$ m^2.

different permeability values, the equivalent phase velocity and inverse quality factor as functions of the frequency. We consider the soft and porous sandstone 1 for the properties of the rock frame, an outer radius $R_w = 0.4$ m, and gas saturations S_g of 0.1 and 0.5. We observe significant attenuation and velocity dispersion effects, particularly in the case of $S_g = 0.1$, with Q values of less than 10. Moreover, we also see that the transition frequency, that is, the frequency associated with the attenuation peak, increases significantly with permeability, which is in agreement with eq. (10). It is also very interesting to note that, while the permeability affects the location of the loss peak and the frequency range where the velocity dispersion takes place, the total amount of attenuation and velocity dispersion does not depend on this parameter. Comparable results were obtained for the harder and less porous sandstone 2, although the attenuation and velocity dispersion levels were, as expected, less significant than for sandstone 1. Similar results were also obtained for a range of outer radii R_w and gas saturations S_g. We observed the same behaviour also in the case of layered media similar to those originally considered by White *et al.* (1975). A general result of this analysis therefore is that, regardless of the size and geometry of the gas–water patches, attenuation and dispersion effects may be significant for a given frequency range for soft and porous formations with gas saturations close to 0.1. In addition, and again in agreement with previous related work (e.g. Carcione & Picotti 2006; Rubino *et al.* 2009), the frequencies at which energy loss and velocity dispersion are at their maxima move towards higher values with increasing permeability.

Next, we study the role of the Johnson parameters on the seismic response of porous media characterized by patchy saturation. Fig. 2 shows, as reference curves, the inverse quality factor and phase ve-

locity corresponding to spherical gas patches with $R_w = 0.4$ m and $S_g = 0.1$. Also, the top and bottom panels in Fig. 2 show the corresponding curves that we obtain by alternatively changing the values of S/V, leaving $T_0 = \kappa T$ unchanged, and T_0, leaving S/V unchanged, respectively. Please note that we use T_0 rather than T, since this parameter is independent of permeability. For the rock frame we use the parameters of sandstone 1 and a permeability of 1 D. Fig. 2(a) shows that the maximum amount of seismic loss decreases, the transition frequency increases and the loss peak widens as the value of S/V, and thus the irregularity of the patches, increases, which is in agreement with the results of Picotti *et al.* (2010). In addition, it is interesting to note that there seems to be a threshold value of S/V beyond which the loss amount remains constant but the attenuation peak keeps moving towards higher frequencies. We also observe in Fig. 2(b) that the parameter S/V affects the velocity dispersion correspondingly: the transition between the low- and high-frequency limits is more abrupt for smaller values of S/V, while it occurs over a wider frequency range for higher values and the velocity increase starts at higher frequencies for larger values of S/V.

Figs 2(c) and (d) show that the seismic response is also very sensitive to the parameter T_0: the maximum loss decreases, the transition frequency gets lower and the loss peak gets wider for increasing T_0; correspondingly, the phase velocity increase occurs along wider frequency ranges and starts at lower frequencies as T_0 increases. As in the case of S/V, we also see that there seems to be a threshold value of T_0 beyond which attenuation and velocity dispersion remain almost constant. The overall behaviour of the inverse quality factor and phase velocity with respect to changes in the parameters S/V and T_0 in the case of the sandstone 2 turned out to be
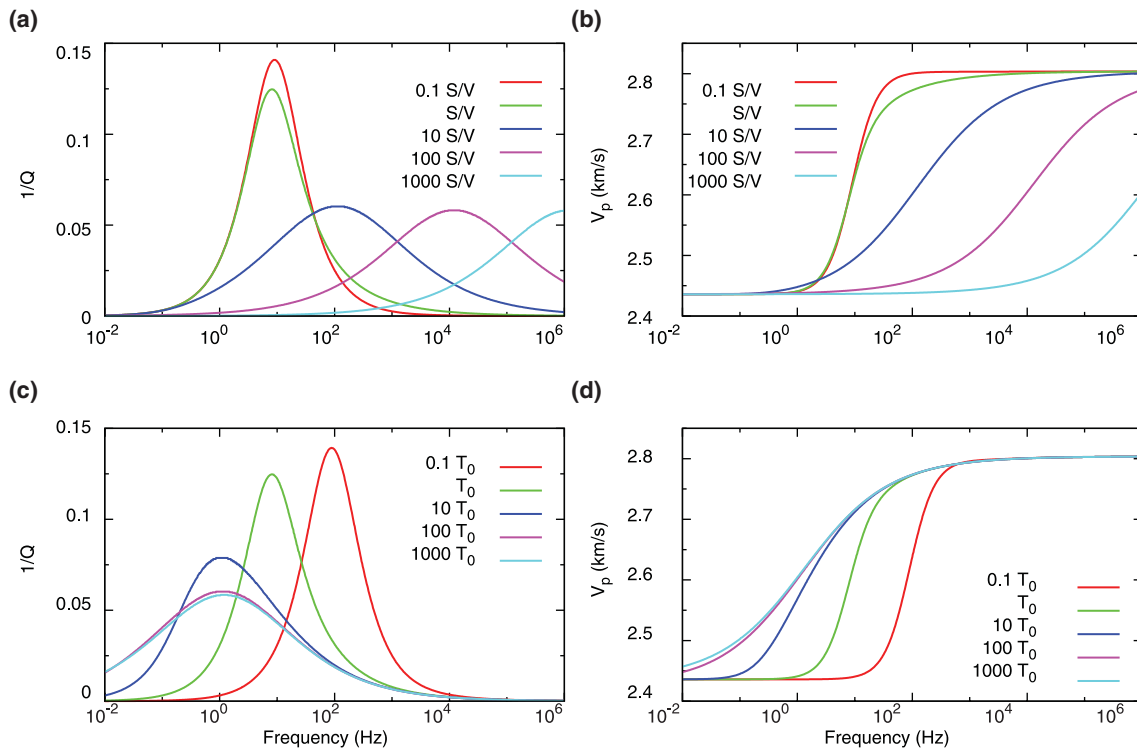

Figure 2. (a,c) Inverse quality factor and (b,d) phase velocity as functions of frequency. Green lines correspond to White's (1975) spherical model considering an outer radius $R_w = 0.4$ m, a gas saturation $S_g = 0.1$ and a permeability $\kappa = 1$ D for sandstone 1 (Table 1). The other curves correspond to the responses obtained for the same model parameters for a range of S/V (top panels) and T_0 values (bottom panels).
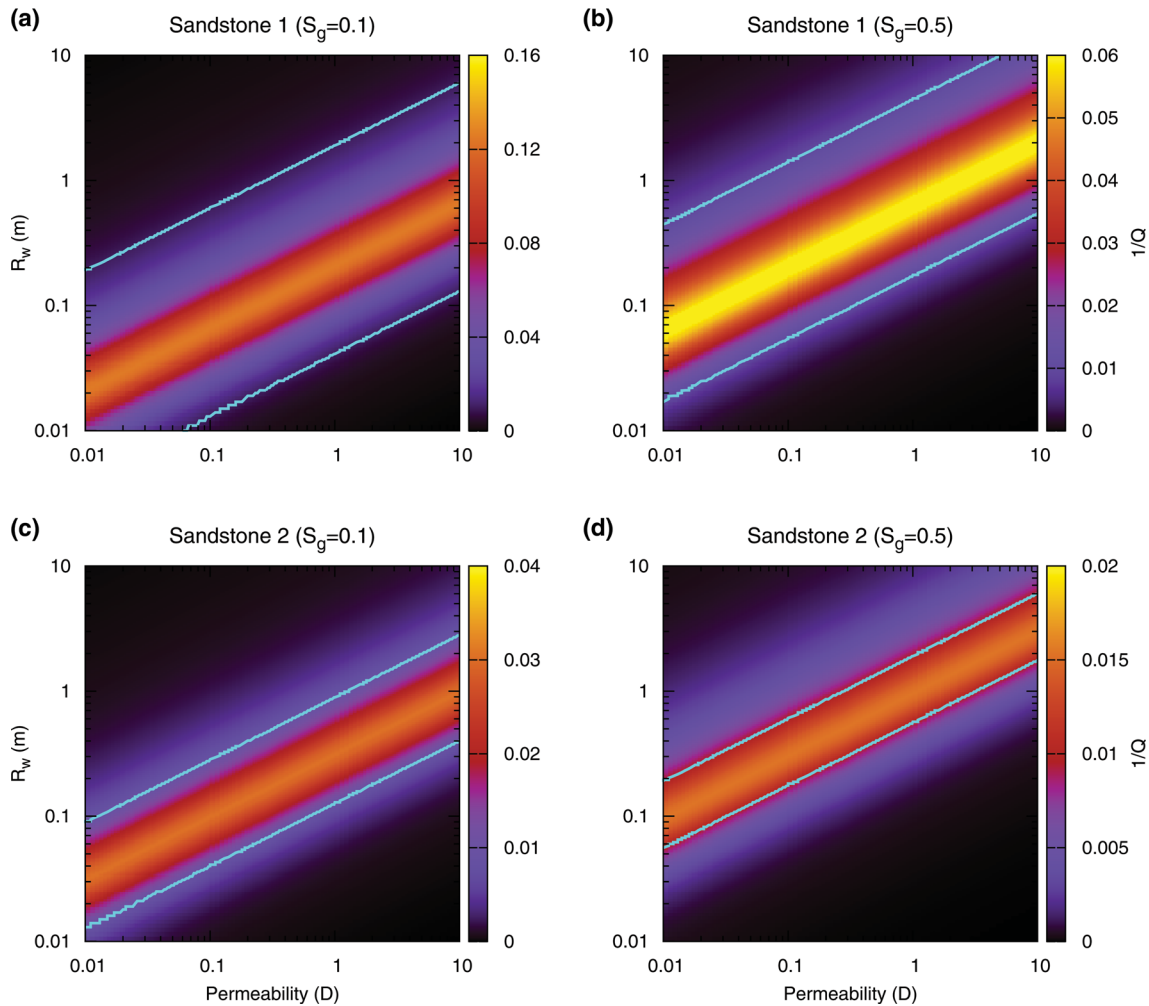
(a)

Sandstone 1 (S_g=0.1)

(b)

Sandstone 1 (S_g=0.5)

(c)

Sandstone 2 (S_g=0.1)

(d)

Sandstone 2 (S_g=0.5)

Figure 3. Inverse quality factor $1/Q$ for a frequency of 30 Hz as a function of permeability and outer radius R_w for spherical gas pockets. Top and bottom panels refer to sandstones 1 and 2, respectively (Table 1). In addition, (a) and (c) correspond to a gas saturation $S_g = 0.1$, while (b) and (d) correspond to $S_g = 0.5$. In all cases, the light blue lines denote $Q = 100$.

exactly the same. As expected, the levels of attenuation and velocity dispersion were, however, less significant and the corresponding results are not shown for brevity.

Since we are interested in studying the role of permeability on surface seismic data, it is important to analyse what kinds of heterogeneity sizes can produce significant wave-induced fluid flow effects in the pertinent frequency range. From eq. (10) we observe that, for a given frequency range, the patch sizes which may produce significant attenuation effects depend strongly on permeability. Fig. 3 shows the inverse quality factor $1/Q$ as function of permeability κ and outer radius R_w for a frequency of 30 Hz in the case of the spherical White's (1975) model. By inspecting Figs 3(a) and (b) we see that, in the case of sandstone 1, the heterogeneity sizes which may produce significant attenuation effects in the typical seismic frequency range, get larger as permeability increases. Moreover, we see that, for suitable combinations of patch sizes and permeabilities, significant attenuation may prevail for both relatively low and relatively high levels of gas saturation ($S_g = 0.1$ and $S_g = 0.5$). As expected from the analysis shown earlier, the attenuation levels for $S_g = 0.1$ are much higher than for $S_g = 0.5$. It is interesting to note that the maximum attenuation level seems to be relatively insensitive to the outer patch radius R_w and permeability κ. We also observe that a remarkably wide range

of patch sizes, from a few centimetres to a few metres, in combination with suitable permeabilities can produce significant attenuation effects.

This in turn indicates that for spherical gas patches having diameters ranging from a few centimetres to a few metres there will be a given permeability range for which attenuation and velocity dispersion effects will be particularly significant at seismic frequencies. In addition, for much smaller permeability values, the transition frequency occurs at much lower values and hence the attenuation will be negligible at seismic frequencies while the corresponding phase velocity will be determined by the high-frequency limit. Conversely, for much higher permeabilities the attenuation will also be negligible but the corresponding phase velocity will be given by the low-frequency limit. These conclusions are corroborated by Fig. 4, which shows the inverse quality factor and phase velocity as functions of permeability for a frequency of 30 Hz. In this particular case, we consider spherical gas pockets with an outer radius $R_w = 0.4$ m and two different levels of gas saturations $S_g = 0.1$ and $S_g = 0.5$. The corresponding results are particularly interesting, since they suggest that for spherical gas pockets with a broad range of diameters seismic waves should contain valuable information about the permeability of the probed formation. Similar results were obtained for sandstone 2 containing spherical gas pockets (Figs 3c and d),
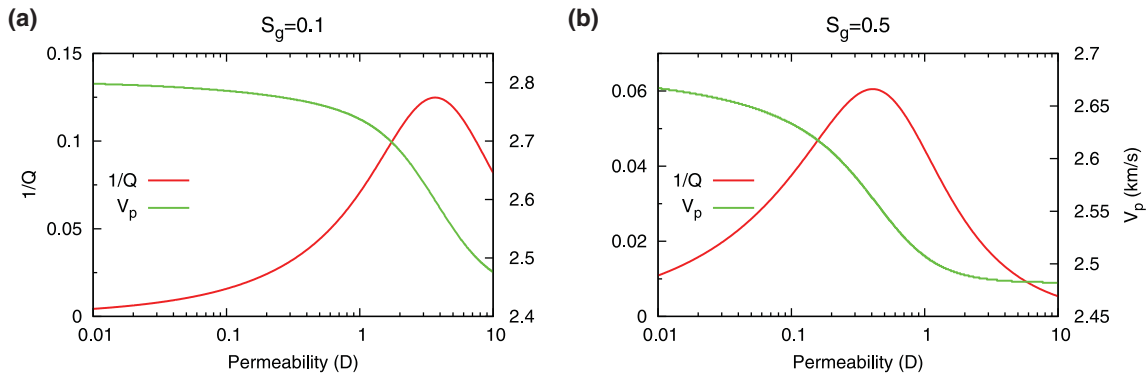
Figure 4. Inverse quality factor and phase velocity as functions of permeability for a frequency of 30 Hz and in the presence of spherical gas pockets ($R_w = 0.4$ m). Dry frame properties correspond to those of sandstone 1 (Table 1) with gas saturations of (a) $S_g = 0.1$ and (b) $S_g = 0.5$.

albeit again with less significant attenuation effects, as well as for the layered model of White *et al.* (1975).

For more general patch patterns, the information about the geometry of the gas patches is characterized by the Johnson parameters T and S/V (Appendix A) and it is therefore interesting to analyse the ranges of these parameters that may produce significant attenu-

ation at seismic frequencies. With this aim, Fig. 5 shows the inverse quality factor for a frequency of 30 Hz as a function of T_0 and S/V for sandstone 1. The top panels correspond to a gas saturation $S_g = 0.1$, while bottom panels correspond to $S_g = 0.5$. The left and right panels show the results for permeability values of $\kappa = 0.01$ and 10 D, respectively. We observe that the range of S/V values
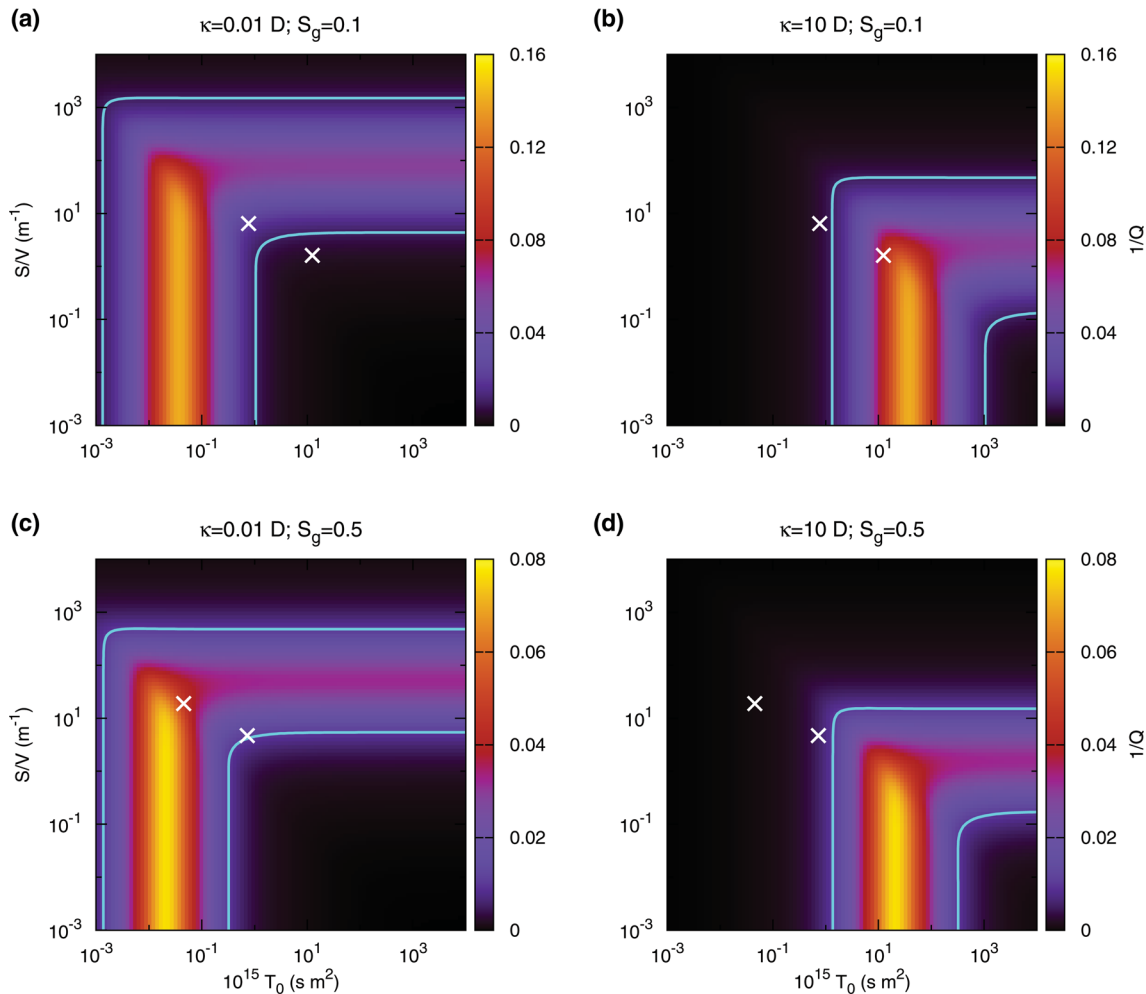

Figure 5. Inverse quality factor $1/Q$ of sandstone 1 (Table 1) for a frequency of 30 Hz as a function of T_0 and S/V. Light blue contour lines correspond to $Q = 100$. In each panel, the white crosses indicate the values of T_0 and S/V corresponding to the spherical patches with $R_w = 0.1$ m (leftmost cross) and $R_w = 0.4$ m (rightmost cross).

that may produce significant attenuation effects decreases with increasing permeability. Conversely, the corresponding dependence on T_0 is more complex. For a given permeability value there is a given range of S/V values for which attenuation effects are significant only for a relatively narrow range of T_0 values. In addition, for a relatively narrow range of S/V values, there is a very wide range of values of T_0 that produce significant attenuation effects. For instance, for $\kappa = 0.01$ D and S/V values in the range $\sim 10^1$ to $\sim 10^3$ m^{-1} all values of T_0 above $\sim 10^{-18}$ sm^2 produce significant attenuation effects for a frequency of 30 Hz. It is important to note here that, although the values of T_0 shown in the panels are smaller than $\sim 10^{-11}$ sm^2, we verified that the inverse quality factor for the mentioned range of S/V remains constant for values of T_0 larger than those shown in the Fig. 5. This can be explained from the fact that the corresponding values of T_0 seem to be above the threshold value suggested by Fig. 2 and hence the response of the medium does not change as the value of T_0 increases further.

The preceding analysis refers to the extreme permeability values 0.01 and 10 D. For intermediate permeability values, the corresponding behaviour is therefore expected to lie between those two cases. Therefore, for each pair of Johnson parameters having values of S/V between $\sim 10^{-1}$ and $\sim 10^3$ m^{-1} with values of T_0 above $\sim 10^{-18}$ sm^2 or having values of S/V below $\sim 10^{-1}$ m^{-1} together

with values of T_0 between $\sim 10^{-18}$ and $\sim 5 \times 10^{-13}$ sm^2, significant attenuation effects can be expected for a certain permeability range within the 0.01–10 D interval for the levels of gas saturation considered in this analysis. It is important to note here that this permeability range will depend on the particular values of the Johnson parameters. These results thus indicate that for the domain of Johnson parameters defined earlier there will be a permeability range for which the attenuation and velocity dispersion effects are significant for frequencies close to 30 Hz. For much smaller permeability values the attenuation will be negligible at these frequencies and the phase velocity will be given by the high-frequency limit. For much higher permeabilities the attenuation will also be negligible, but the corresponding phase velocity will be given by the low-frequency limit. This in turn suggests that for reservoirs with patchy saturation and Johnson parameters lying in the previously defined ranges, seismic data should contain information on the permeability of the probed formation.

Comparable results were also obtained for the behaviour of the inverse quality factor as a function of the Johnson parameters for the sandstone 2, though, as expected, the levels of attenuation turned out to be again less significant (Fig. 6). Correspondingly, the ranges of values of T_0 and S/V for which attenuation effects are important are narrower than for sandstone 1.
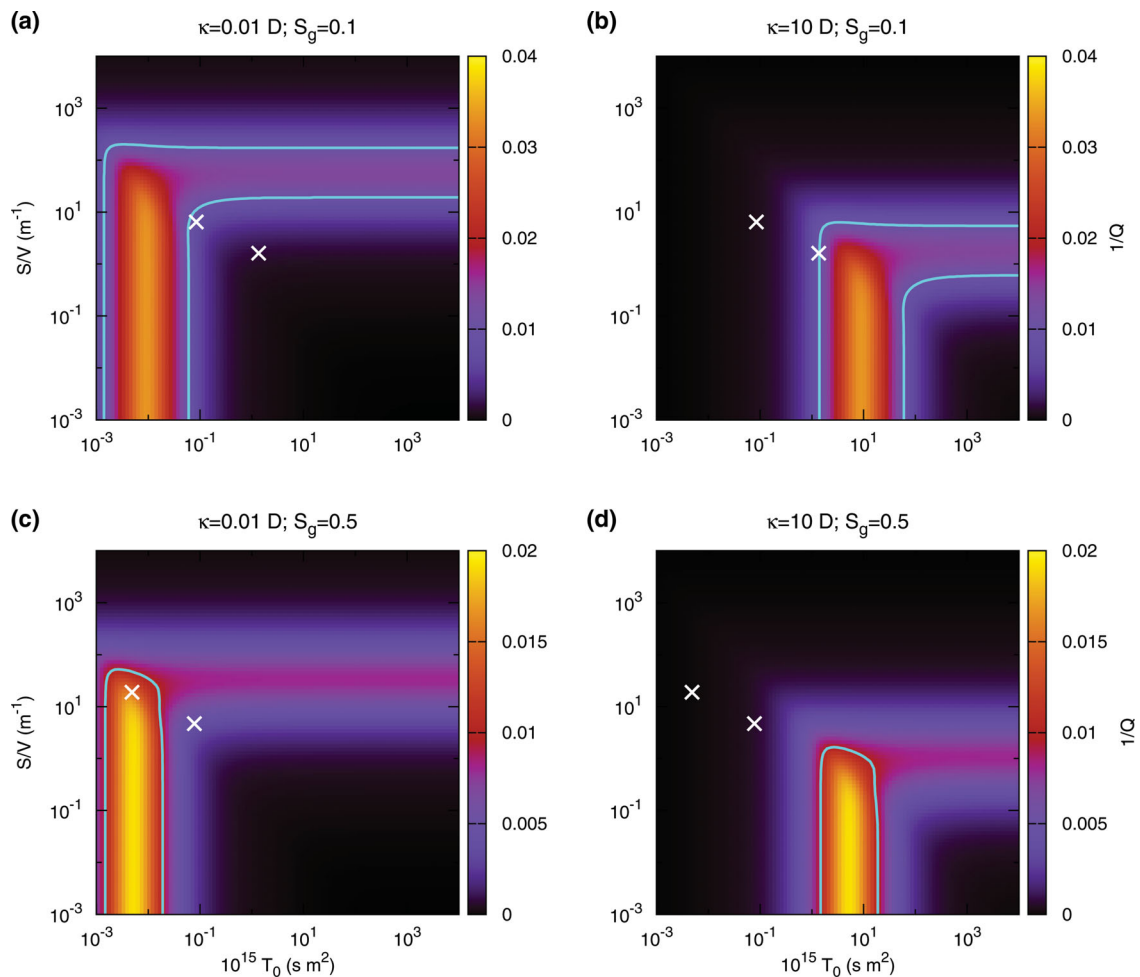

Figure 6. Inverse quality factor $1/Q$ of sandstone 2 (Table 1) for a frequency of 30 Hz as a function of T_0 and S/V. Light blue contour lines correspond to $Q = 100$. In each panel, the white crosses indicate the values of T_0 and S/V corresponding to the spherical patches with $R_w = 0.1$ m (leftmost cross) and $R_w = 0.4$ m (rightmost cross).

3 PERMEABILITY EFFECTS ON SEISMIC WAVES REFLECTED FROM A PLANE INTERFACE

Recently, Ren *et al.* (2009) analysed the dependence of normal-incidence reflection coefficients on permeability for gas reservoirs consisting of a stack of thin layers alternately fully saturated with gas and water (White *et al.* 1975) and found that permeability can indeed affect the amplitudes of the reflected waves significantly. This study considered low- and high-impedance reservoir models. In both cases the individual layers had constant thickness of 1 m. In the following, we seek to extend and generalize this research effort by building on the results of our preceding attenuation and velocity dispersion analysis and by considering various patch geometries and gas saturation scenarios to better understand the role of permeability on seismic reflection data for gas reservoir models. With this aim, we quantify the normal-incidence reflectivity variations at the top of a gas reservoir for a wide range of patch geometries and gas saturations as functions of permeability. In addition, we analyse the permeability effects on non-normal-incidence data, including reflected *S* waves, and assess the potential importance of amplitude-versus-angle (AVA) data in these kinds of studies.

Performing numerical simulations of poroelastic seismic wave propagation in the presence of mesoscopic heterogeneities is computationally very expensive. This is due to the fact that the diffusion lengths associated with the pore fluid pressure equilibration processes at the heterogeneities are very small compared with the predominant seismic wavelengths, which in turn mandates excessively small discretization levels (Rubino *et al.* 2007). To obtain the AVA response of the considered reservoir models, we therefore employ Johnson's (2001) model to replace the corresponding sandstones with patchy saturation by equivalent viscoelastic solids and solve the viscoelastic equations of motion in the space–frequency domain for the case of a plane wave striking the top of the reservoir at a given incidence angle. The corresponding equivalent viscoelastic solids have the same bulk density, attenuation, and velocity dispersion as the original patchy-saturated medium and thus implicitly include the mesoscopic effects expected to arise in these environments. This approach, which is similar to that employed by Rubino & Velis (2011) to obtain the AVA response of a thin layer with patchy saturation, is very convenient, since for the same order of accuracy solving the viscoelastic equations of motion is computationally much less expensive than any numerical procedure based on the discretization of Biot's (1956b) equations. Appendix B describes the details of this numerical procedure. Please note that while this approach ignores the generation of slow *P* waves at the interface separating the reservoir and the corresponding caprock, it does indeed fully account for the energy converted to slow waves at the mesoscopic heterogeneities lying within the reservoir. Moreover, Quintal *et al.* (2009) found good agreement between the normal-incidence reflections from a partially saturated thin layer obtained considering equivalent viscoelastic solids and those determined solving the Biot's (1956b) equations of motion. This in turn indicates that the amount of energy converted into slow *P* waves at the shale–reservoir interface is likely to be very small, and hence essentially insignificant for the purpose of our work.

For the following analysis, we use a Ricker wavelet with a peak frequency f_0 of 30 Hz and consider a planar horizontal interface separating a sandstone reservoir characterized by patchy saturation and a shaly caprock. As in the previous section, we consider two kinds of sandstones for the reservoir (Table 1): a highly porous and soft formation (sandstone 1), and a harder and less porous

formation (sandstone 2). For the shale caprock, we use the properties of the overburden shale of the reservoir model employed by Liu *et al.* (2011), which corresponds to an elastic medium with $V_p = 2.65 \, \text{km s}^{-1}$, $V_s = 1.16 \, \text{km s}^{-1}$ and $\rho = 2.27 \, \text{g cm}^{-3}$. Please note that the stiffness of this non-dispersive rock lies between those of the two reservoir sandstones.

3.1 White's spherical model

We first analyse the behaviour of the seismic reflection responses from reservoir models characterized by spherical gas patches (White 1975). We consider two different angles of incidence $\theta = 0°$ and $\theta = 30°$, two gas saturation levels $S_g = 0.1$ and 0.5, and several permeability values κ in the range between 0.01 and 10 D. Figs 7 and 8 show the reflected compressional waves for the soft gas reservoir model (sandstone 1 overlain by shale) with outer radii R_w of 0.4 and 0.1 m, respectively. In general, there is a significant dependence of the responses on permeability, especially for low gas saturation: the greater the permeability, the greater the reflected trace absolute amplitude for all incidence angles and gas pocket sizes considered. The observation that the reflectivity increases with permeability at the top of a gas reservoir that is softer than its caprock is indeed in agreement with the results of Ren *et al.* (2009). This behaviour can be understood by analysing Fig. 4, which shows that, in general, there is a decrease of phase velocity with increasing permeability. Thus, there is a decrease of the acoustic impedance of the gas reservoir with increasing permeability, which, in the case of a gas reservoir that is softer than its caprock, will produce an increase of the reflection coefficient with permeability. In this context, it is interesting to note the low amplitude of the trace associated with $\kappa = 0.01$ D and $S_g = 0.1$ depicted in Fig. 7(a). Here, the resulting reflection coefficient is very small and thus there is almost no energy reflected at normal incidence. The low reflectivity can be explained by the fact that for this permeability, gas saturation, and pocket size, the compressional phase velocity in the vicinity of the dominant frequency is almost equal to the high-frequency limit (Fig. 1b). The resulting seismic impedance for this reservoir is then almost equal to the impedance of the caprock and therefore the effective reflection coefficient for $\theta = 0$ is very small. However, when the permeability increases, the attenuation peak moves towards higher frequencies and so does the frequency range where the velocity dispersion occurs. As a consequence, the velocity decreases for the frequencies contained in the wavelet (Fig. 4), the impedance contrast increases, and the reflected wave becomes apparent. A similar behaviour is observed for $R_w = 0.1$ m (Fig. 8a). Figs 7 and 8 also show that the sensitivity of the seismic responses to permeability tends to be less significant for higher gas saturation and that the behaviour of the non-normal-incidence traces is similar to those of the normal-incidence ones, although the magnitude of their amplitudes is very different.

It is also interesting to note that, besides the observed amplitude variation with permeability, the shape of the reflected wave changes with regard to the symmetrical Ricker-type source wavelet for certain permeability values. In the case of low gas saturation (Figs 7a and b and 8a and b), the largest wavelet deformations are observed for κ values of 1 and 0.1 D when the outer radii R_w are 0.4 and 0.1 m, respectively. This effect is associated with the relationship between the frequency range at which the attenuation peak and maximum velocity dispersion take place and the permeability (eq. 10). In effect, Fig. 1(a) shows that the maximum attenuation occurs in the vicinity of $f_0 = 30$ Hz for $\kappa = 1$ D and $R_w = 0.4$ m. Though
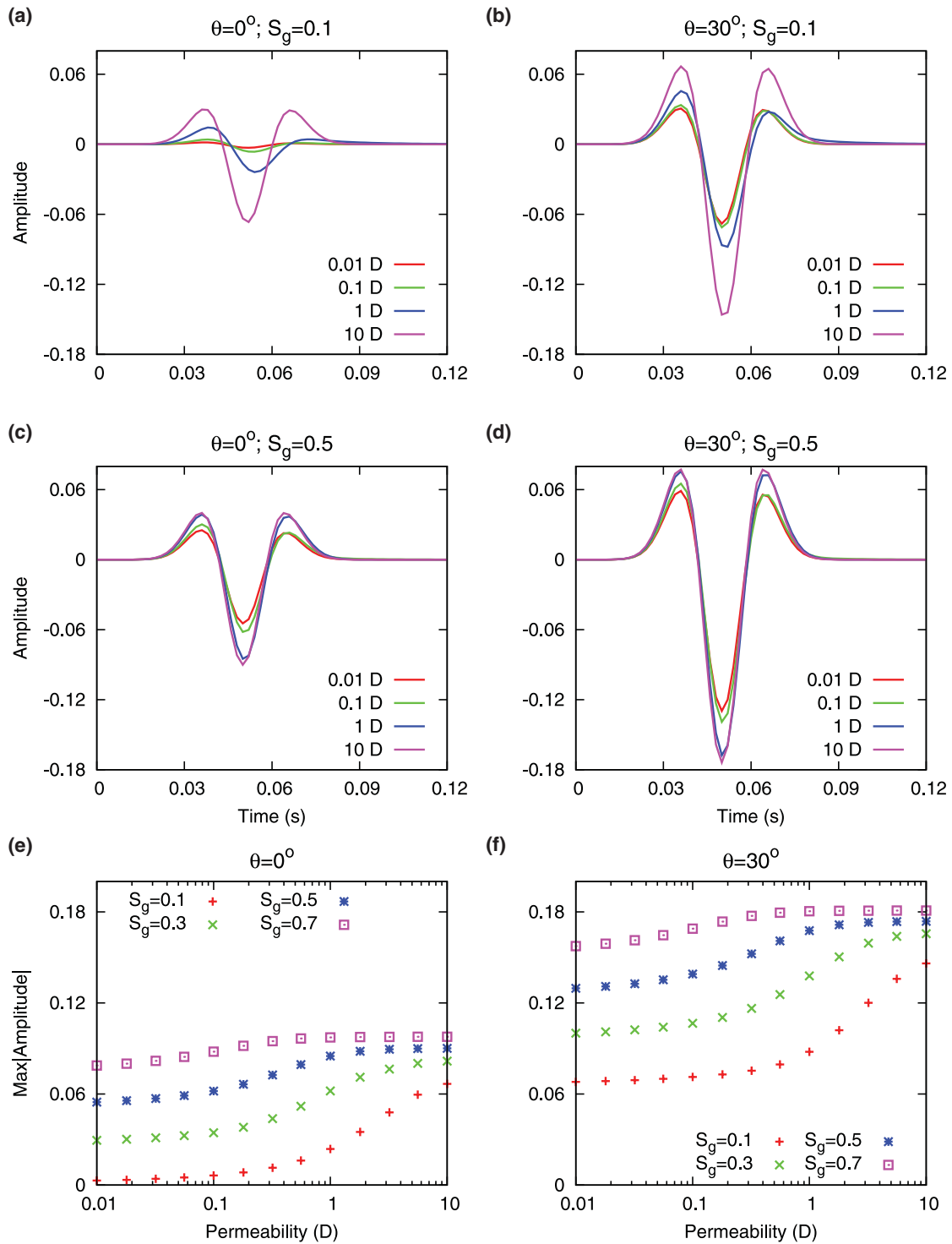
Figure 7. (a–d) Reflected waveforms from the interface between shale and sandstone 1 (Table 1) and (e and f) corresponding maximum absolute amplitudes for various permeability values and $R_w = 0.4$ m. Left-hand column: incidence angle $\theta = 0°$; right-hand column: incidence angle $\theta = 30°$; top row: $S_g = 0.1$; middle row: $S_g = 0.5$.

not shown for brevity, maximum attenuation is also observed in the vicinity of $f_0 = 30$ Hz for $\kappa = 0.1$ D and $R_w = 0.1$ m. Therefore, the observed deformation of the reflected wavelet represents a direct consequence of the attenuation and velocity dispersion effects on the data.

Figs 9 and 10 show the reflected compressional waves for the hard gas reservoir model (sandstone 2 overlain by shale) with R_w

values of 0.4 and 0.1 m, respectively. In general, and in contrast to the previously considered case of a soft gas reservoir, there is no significant variation of the reflection responses with permeability at normal incidence. However, the variation is significant for non-normal incidence and low gas saturations. In addition, it is interesting to note that, as opposed to the soft reservoir case, the reflected absolute amplitude decreases with increasing permeability
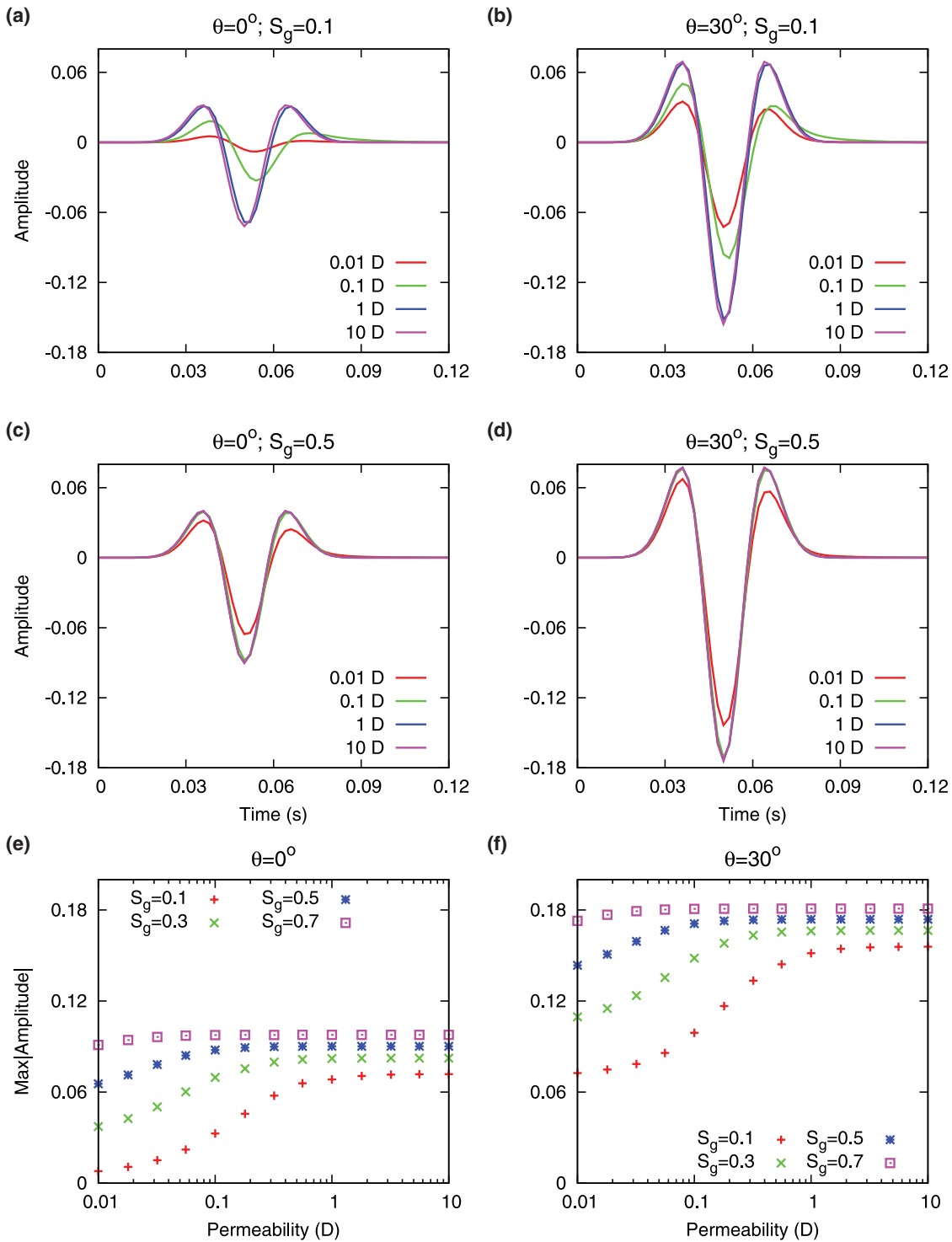
Figure 8. (a–d) Reflected waveforms from the interface between shale and sandstone 1 (Table 1) and (e and f) corresponding maximum absolute amplitudes for various permeability values and $R_w = 0.1$ m. Left-hand column: incidence angle $\theta = 0°$; right-hand column: incidence angle $\theta = 30°$; top row: $S_g = 0.1$; middle row: $S_g = 0.5$.

regardless of the angle of incidence, gas saturation or gas pocket size. The observation that the reflectivity decreases when the permeability increases in gas reservoirs that are stiffer than the overlying caprock is again consistent with the results of Ren *et al.* (2009). This behaviour can also be explained from the fact that, as shown in the Fig. 4 for the soft sandstone, the compressional phase velocity of sandstone 2 is expected to decrease with permeability, which in

the case of a softer caprock will produce a decrease of the acoustic impedance contrast and, equivalently, a decrease of the reflection coefficient with permeability.

It is important to mention here that, despite the fact that the reflected waves show a significant sensitivity to permeability in most of the cases analysed, this sensitivity is limited to a certain permeability range. This becomes evident by inspecting Figs 7(e)
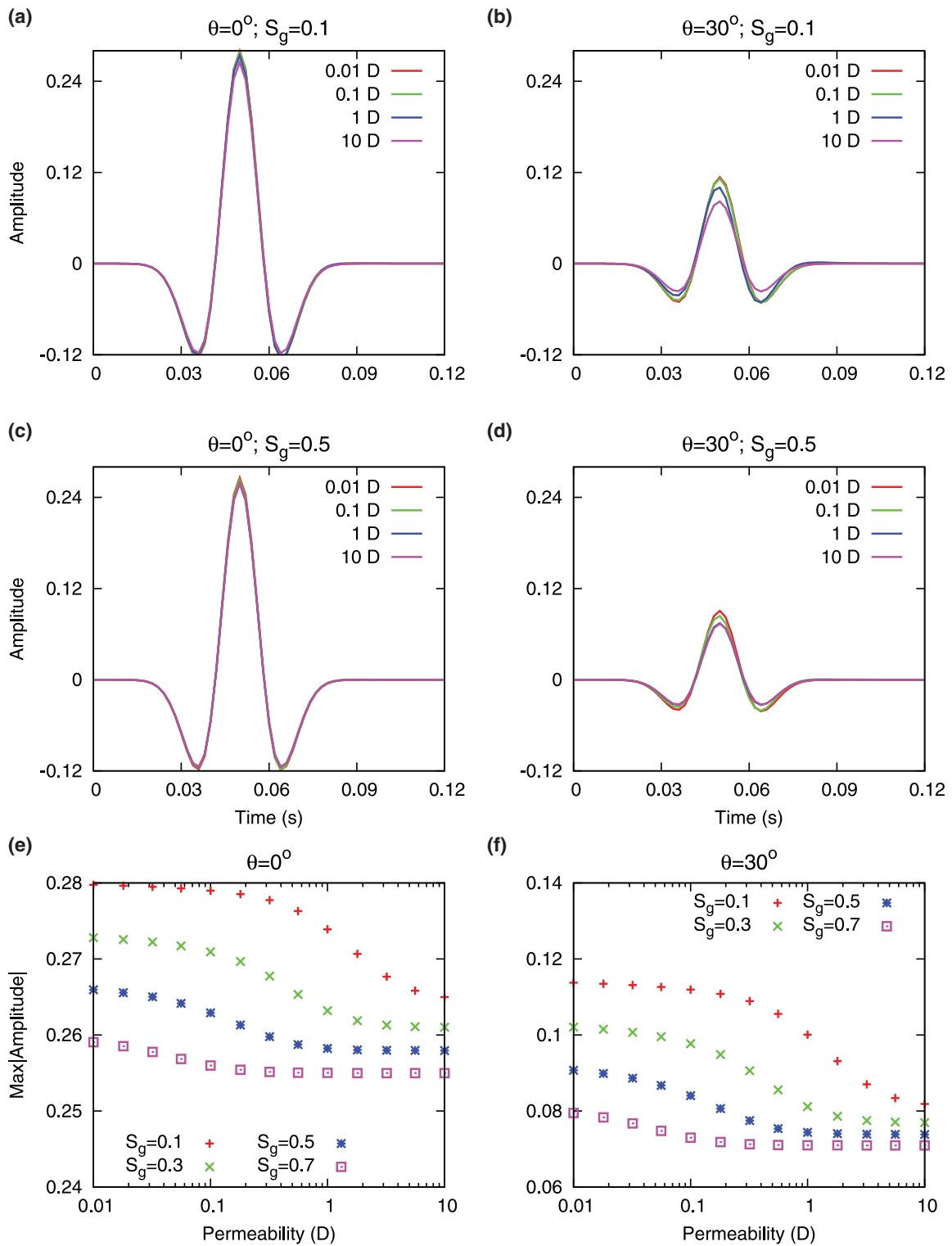
Figure 9. (a–d) Reflected waveforms from the interface between shale and sandstone 2 (Table 1) and (e and f) corresponding maximum absolute amplitudes for various permeability values and $R_w = 0.4$ m. Left-hand column: incidence angle $\theta = 0°$; right-hand column: incidence angle $\theta = 30°$; top row: $S_g = 0.1$; middle row: $S_g = 0.5$.

and (f), 8(e) and (f), 9(e) and (f) and 10(e) and (f), where we can see that the curves flatten for certain permeability ranges. In general, this flattening occurs towards the lower (0.01–0.1 D) or/and upper (1–10 D) ends of the considered permeability range, where the amplitude changes become negligible for certain gas satura-

tions and patch sizes. In all cases, however, there is a permeability range where amplitude variations occur and these variations may be particularly significant for some gas saturations. These results are in agreement with the analysis shown in Fig. 4, which illustrates that the phase velocity decreases from the high-frequency
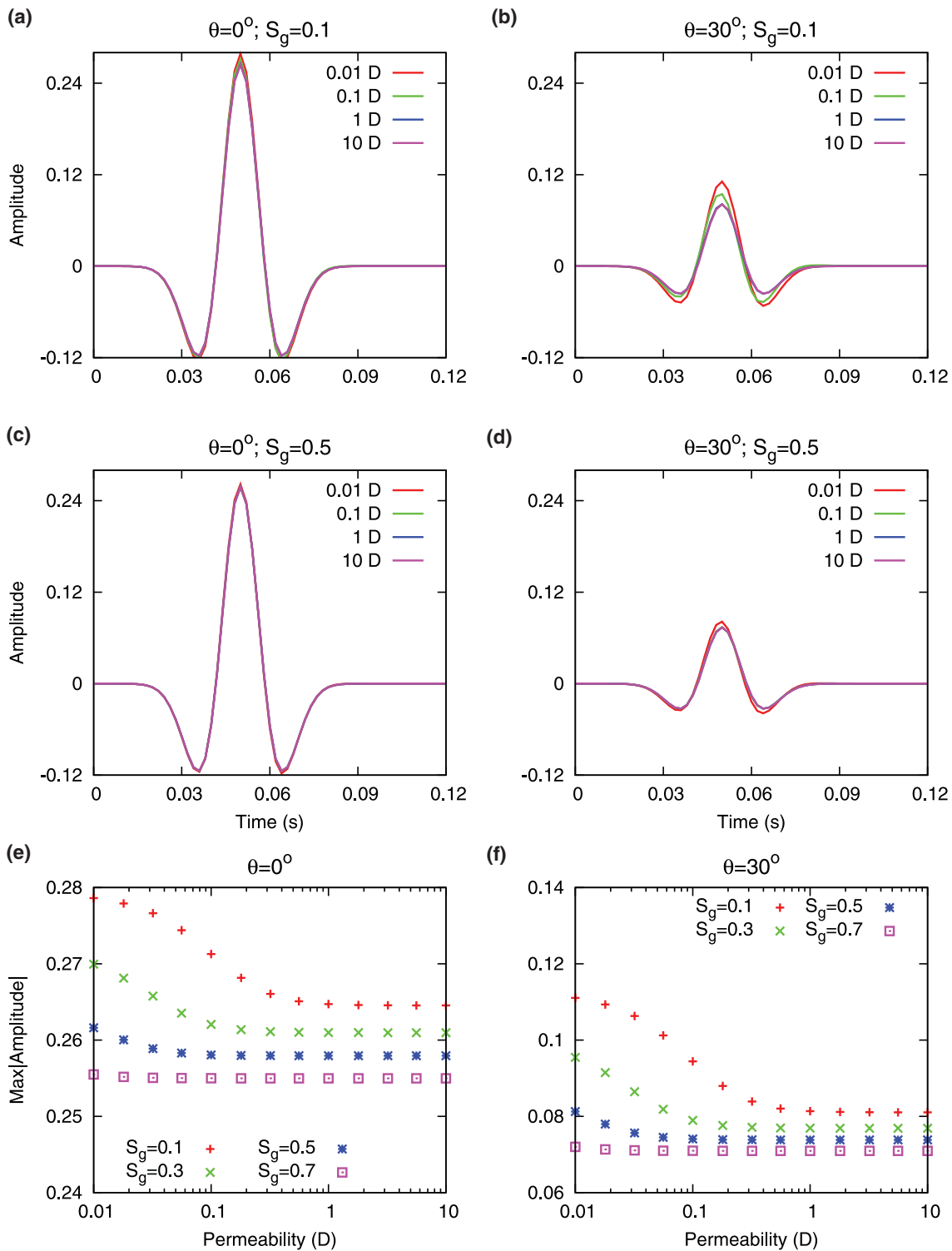
Figure 10. (a–d) Reflected waveforms from the interface between shale and sandstone 2 (Table 1) and (e and f) corresponding maximum absolute amplitudes for various permeability values and $R_w = 0.1$ m. Left-hand column: incidence angle $\theta = 0°$; right-hand column: incidence angle $\theta = 30°$; top row: $S_g = 0.1$; middle row: $S_g = 0.5$.

limit value to the low-frequency limit value within a relatively narrow permeability range, where most of the seismic attenuation also takes place. These velocity changes and attenuation effects lead to the observed variations in the absolute amplitude of the reflected waves within the corresponding permeability range. On the other hand, for those permeabilities for which there are no significant

velocity dispersion effects within the pertinent spectral bandwidth, the quality factor assumes large values and hence seismic reflection data are not expected to show a significant dependence on permeability.

We repeated all the simulations for the reflected shear waves and observed that their variations with permeability were negligible.
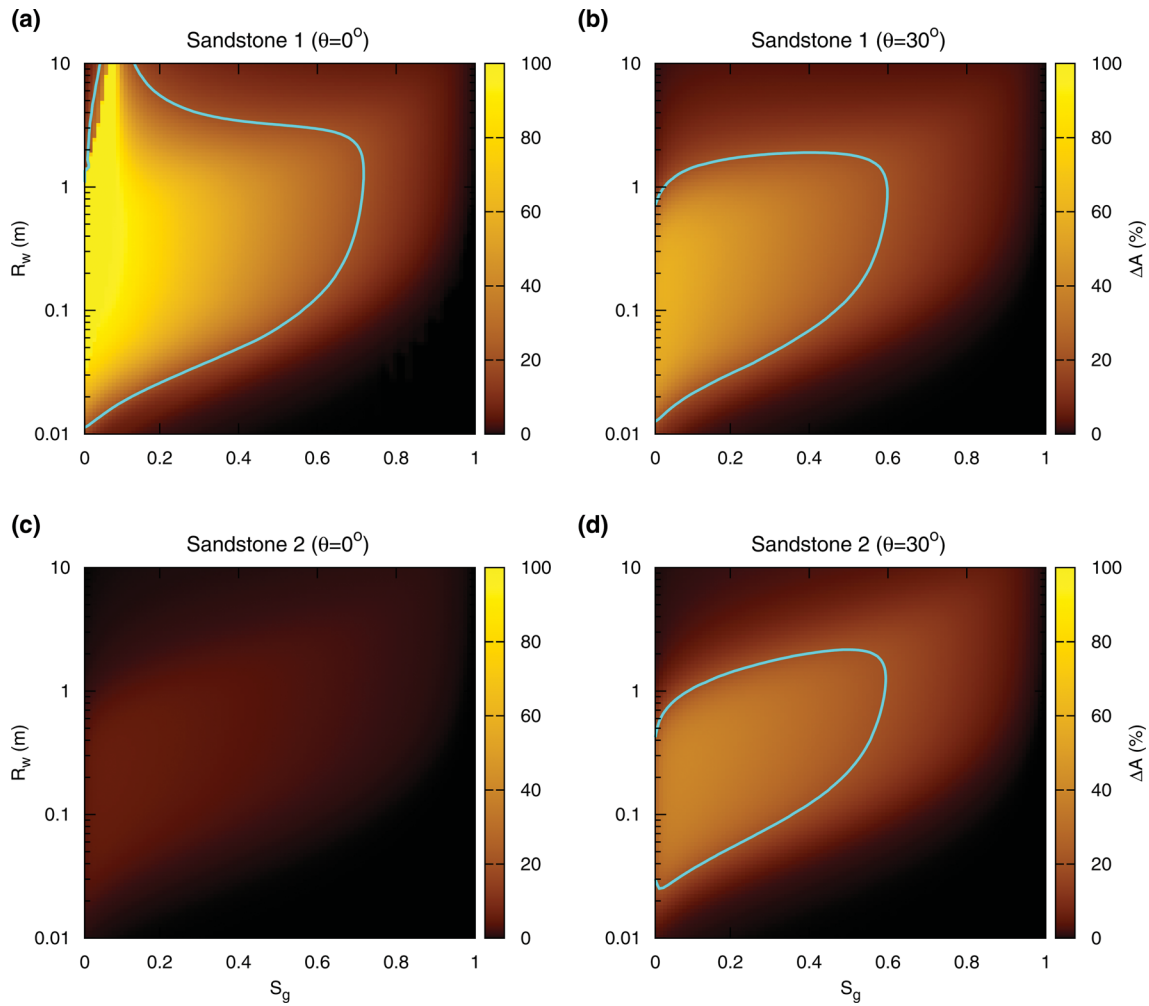
(a)

Sandstone 1 (θ=0°)

(b)

Sandstone 1 (θ=30°)

(c)

Sandstone 2 (θ=0°)

(d)

Sandstone 2 (θ=30°)

Figure 11. Relative difference between the maximum absolute amplitudes of the reflections ΔA (eq. 16) for $\kappa = 0.01$ and 10 D as a function of gas saturation S_g and outer radius R_w for (a) and (b) sandstone 1 (Table 1) overlain by shale and (c) and (d) sandstone 2 overlain by shale. Two different incidence angles are considered: (a and c) $\theta = 0°$ and (b and d) $\theta = 30°$. In all cases, the light blue contour lines correspond to $\Delta A = 20$ per cent.

Similarly, we also repeated this analysis for a stack of porous layers alternately saturated with gas and water (White *et al*. 1975) and found that the corresponding results were indeed almost identical to those for the White's spherical model.

To explore the characteristics of the spherical gas patches that may produce seismic responses sensitive to permeability within the considered permeability range, we calculate the traces associated with the reflections on the top of the two gas reservoirs for wide ranges of gas saturation S_g and outer radii R_w and for two extreme values of permeability κ (0.01 and 10 D). In addition to this, we consider two incidence angles θ (0° and 30°) and, in each case, compute the maximum absolute amplitude of the corresponding traces and analyse its variation with permeability. Since the maximum absolute amplitude as a function of permeability is expected to be a monotonic curve (Figs 7e and f, 8e and f, 9e and f, and 10e and f), we calculate the relative difference ΔA between the maximum absolute amplitudes of the reflections for the two extreme permeability values

$$\Delta A = \frac{|A_2 - A_1|}{\max(A_1, A_2)} \times 100 \text{ per cent,} \qquad (16)$$

where A_1 and A_2 are the maximum absolute amplitudes of the reflections for $\kappa_1 = 0.01$ and $\kappa_2 = 10$ D, respectively. This quantity

is viewed as a measure of the sensitivity of the seismic reflection data to permeability.

Figs 11(a)–(d) show ΔA for the two gas reservoirs for all possible gas saturations S_g and outer radii R_w between 0 and 10 m. These plots are interesting because they allow for determining the patch sizes and gas saturation values that may produce seismic responses sensitive to permeability in the range from 0.01 to 10 D. Except in the case of Fig. 11(c), we observe that, as expected, the sensitivity of the reflected waves to permeability is higher for low gas saturation values. This result is in agreement with the fact that attenuation and velocity dispersion effects are more significant for low gas saturation. In addition, we can see that in the case of sandstone 1 the sensitivity to permeability may be significant even for relatively high gas saturations. For normal incidence, for example, relative differences in excess of 20 per cent are expected for gas saturations as high as 0.6, provided that the outer radii R_w of the gas patches are in the range of tens of centimetres to a few metres. For non-normal incidence, the sensitivity decreases slightly.

Conversely, for sandstone 2 case the sensitivity of normal-incidence data to permeability is very small (Fig. 11c). However, it is relatively significant for non-normal incidence data (Fig. 11d). In fact, the relative differences are similar to those obtained for the non-normal-incidence data in the case of sandstone 1 (Fig. 11b),

which clearly points to the potential of AVA data in the hydraulic characterization of gas reservoirs.

Finally, it is important to note that, although not shown, almost all maximum absolute amplitudes of the seismic reflection data are significant, at least for some permeability values within the considered 0.01–10 D range. However, within the small region approximately defined by $S_g < 0.1$ and $R_w > 1$ m in Fig. 11(a), the maximum absolute amplitudes are below 0.01 for all the considered permeabilities. In all other cases, the maximum absolute amplitudes of the seismic reflection data are larger than this value.

3.2 Johnson's model

To allow for more general gas patch geometries, we now simulate the seismic traces associated with reflections from the top of the two gas reservoirs for a wide range of Johnson parameters and calculate the relative difference between the maximum absolute amplitudes of the reflections for $\kappa = 0.01$ and 10 D as a function of T_0 and S/V. We again consider two different angles of incidence θ (0° and 30°) and two different gas saturations S_g (0.1 and 0.5). The corresponding results are shown in Figs 12 and 13. In the case of Fig. 12 (sandstone 1), we can observe large amplitude variations with permeability

for a wide range of Johnson parameters, especially for low gas saturation. In these cases, we observe variations in the reflection absolute amplitudes of up to 100 per cent (Fig. 12a). This result is in agreement with those shown in Figs 7(a) and 8(a), where we plot the traces corresponding to the spherical gas pocket model at normal incidence and $S_g = 0.1$, for $R_w = 0.4$ and 0.1 m, respectively. In those cases, for $\kappa = 0.01$ D the resulting impedance contrast is very small and thus the amplitude of the reflected wave is almost zero. On the other hand, the contrast increases significantly for $\kappa = 10$ D and thus the absolute amplitudes exhibit large variations over the considered permeability range. These effects decrease when the gas saturation increases (Figs 12c and d) and for non-normal incidence (Figs 12b–d), but the relative differences are still above 20 per cent for a wide range of Johnson parameters.

In the case of sandstone 2, the sensitivity to permeability of the seismic response is, as expected, less significant (Fig. 13). However, it is worth noting that there is a relatively wide range of patchy models that yield relatively large (>20 per cent) absolute amplitude variations ΔA for $\theta = 30°$, regardless of whether the gas saturation S_g is 0.1 or 0.5 (Figs 13b and d). Moreover, it is interesting to note that the sensitivity is larger for the non-normal-incidence case than for the normal-incidence case. This again serves to demonstrate
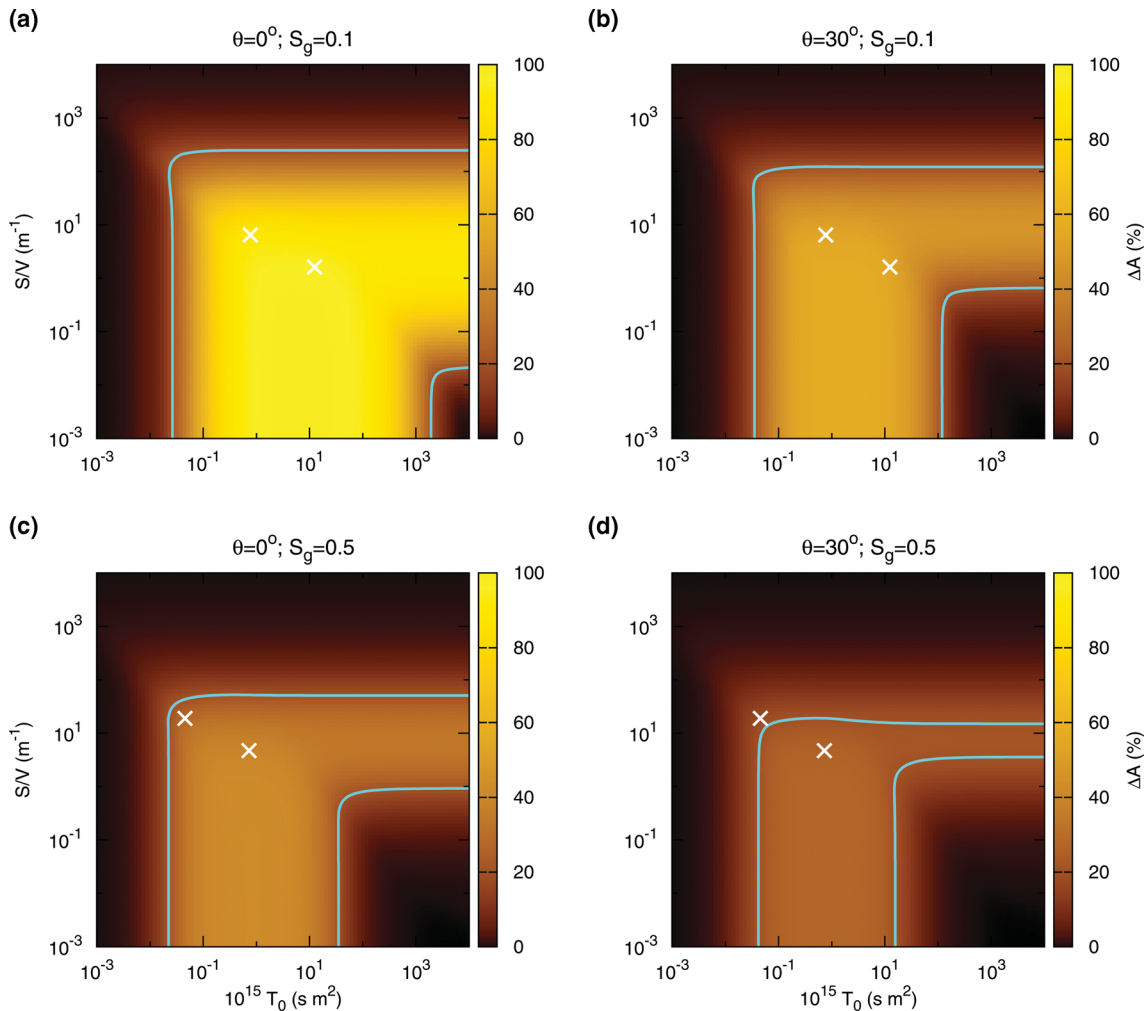

Figure 12. Relative difference between the maximum absolute amplitudes of the reflections ΔA (eq. 16) for $\kappa = 0.01$ and 10 D as a function of Johnson parameters T_0 and S/V in the sandstone 1 (Table 1). Two different incidence angles ($\theta = 0°$ and $\theta = 30°$) and gas saturations ($S_g = 0.1$ and $S_g = 0.5$) are considered. The white crosses correspond to the White's (1975) spherical model with $R_w = 0.1$ m (leftmost cross) and $R_w = 0.4$ m (rightmost cross). In all cases, the light blue contour lines correspond to $\Delta A = 20$ per cent.
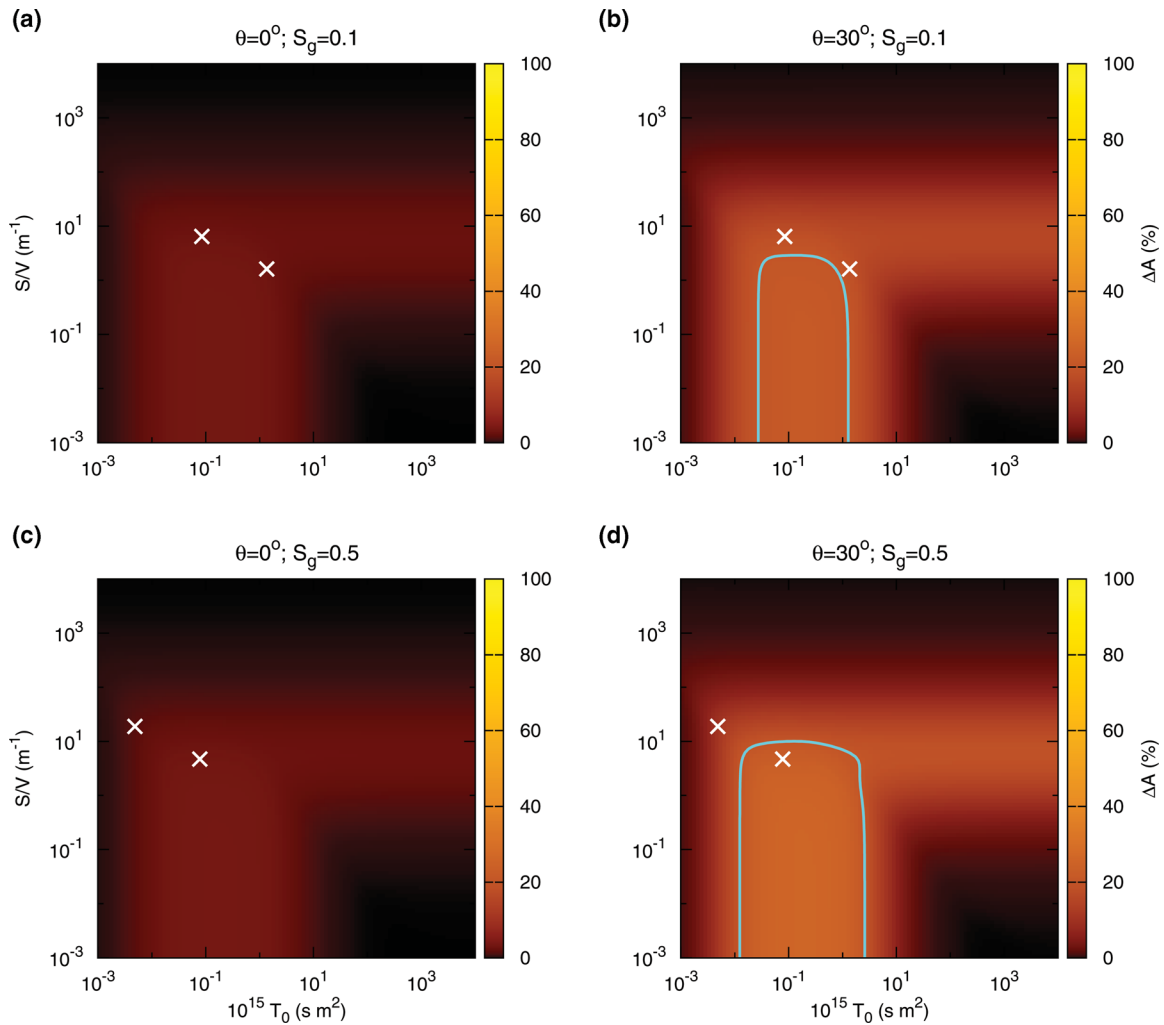
Figure 13. Relative difference between the maximum absolute amplitudes of the reflections ΔA (eq. 16) for $\kappa = 0.01$ and 10 D as a function of Johnson parameters T_0 and S/V in the sandstone 2 (Table 1). Two different incidence angles ($\theta = 0°$ and $\theta = 30°$) and gas saturations ($S_g = 0.1$ and $S_g = 0.5$) are considered. The white crosses correspond to the White's (1975) spherical model with $R_w = 0.1$ m (leftmost cross) and $R_w = 0.4$ m (rightmost cross). In all cases, the light blue contour lines correspond to $\Delta A = 20$ per cent.

that in particular AVA data may contain useful information about the permeability of gas reservoirs.

As for the case of spherical gas pocket (sandstone 1), there is a small range of parameters defined by $T_0 \gtrsim 10^{-9}$ sm^2 and $S/V \lesssim 0.5$ m^{-1} for which the maximum absolute amplitudes of the normal-incidence reflection data are below 0.01 and the meaning of ΔA becomes less important. In all other cases, including all scenarios considered for sandstone 2, the maximum absolute amplitudes are larger than 0.01.

4 PERMEABILITY EFFECTS ON SEISMIC REFLECTION IMAGES

In the previous section, we have analysed the seismic reflectivity at plane interfaces associated with the top of gas reservoirs and observed that it may be significantly affected by the permeability of the reservoir. In addition to this, the compressional waves associated with a given surface-based seismic experiment will also be affected by attenuation and velocity dispersion as they travel through the gas reservoir itself and hence these effects, which are also permeability-dependent, will be present in the recorded traces as well. To explore

these effects, we perform 1-D numerical simulations of seismic wave propagation using the methodology of Rubino *et al.* (2011) to obtain the normal-incidence seismic response of gas reservoirs. As before, we employ Johnson's (2001) model to replace the porous medium characterized by patchy saturation through an equivalent viscoelastic solid and solve the viscoelastic equations of motion in the space–frequency domain.

We consider a very simple 2-D gas reservoir, which consists of a horizontal sandstone layer with thickness of 300 m and spherical gas pockets with $R_w = 0.4$ m embedded between two shale layers of 200 m thickness. The properties for the shales correspond to those of the caprock in the previous section, while the properties of the gas reservoir correspond to those of sandstone 1 (Table 1). Since we are interested in analysing the permeability effects on the seismic data, we consider lateral variations of the reservoir permeability while keeping all other physical properties constant.

Figs 14(a) and (b) show the seismic responses for gas saturation levels $S_g = 0.1$ and $S_g = 0.5$, respectively. It is interesting to observe how the reflectivity associated with the top of the reservoir, located at a time of $\sim$0.2 s, increases with reservoir permeability, which is in agreement with the behaviour we
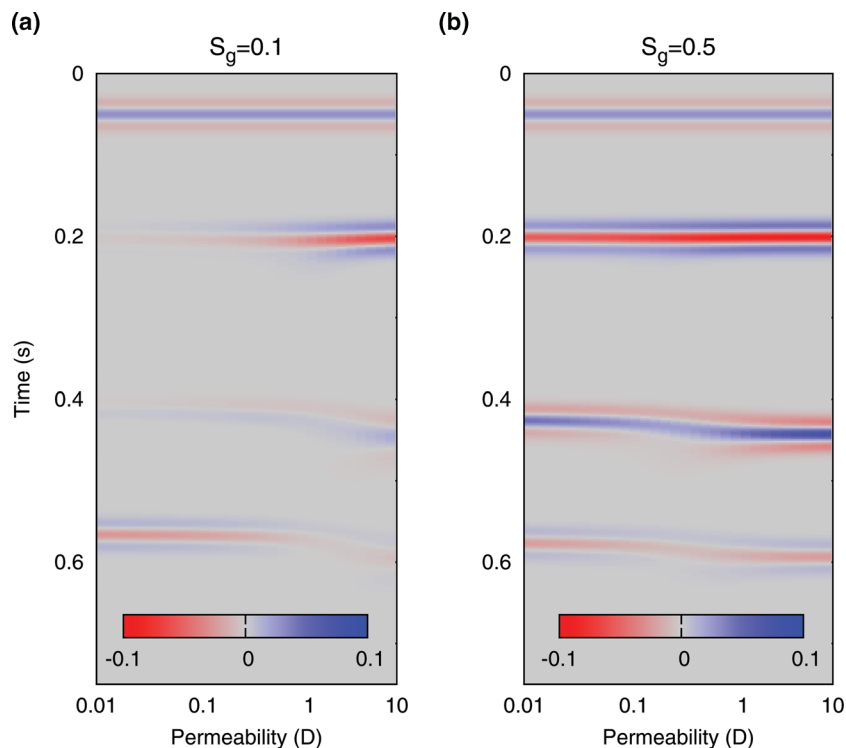
Figure 14. Normal-incidence seismic response of a sandstone gas reservoir containing spherical gas pockets ($R_w = 0.4$ m) for gas saturations (a) $S_g = 0.1$ and (b) $S_g = 0.5$. The reservoir has lateral variations of its permeability and is embedded between two horizontal shale layers. The dry frame properties of the reservoir rock correspond to those of sandstone 1 (Table 1).
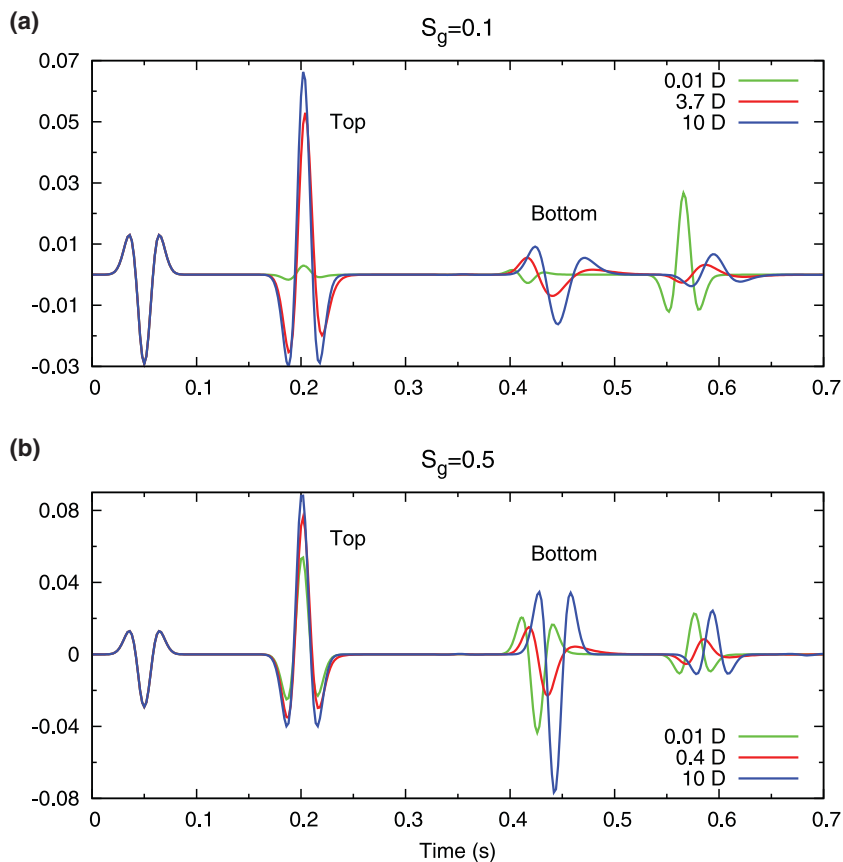

Figure 15. Normal-incidence seismic response of the gas reservoir shown in Fig. 14 for three different permeability values and gas saturations of (a) $S_g = 0.1$ and (b) 0.5. The dry frame properties of the reservoir rock correspond to those of sandstone 1 (Table 1).

observe in Fig. 7. As expected, this effect is much more prominent for low gas saturation. Also, note that the reflection corresponding to the bottom of the reservoir, located at a time of ∼0.4 s, experiences a pushdown in both cases as permeability increases. This is due to velocity dispersion effects, since as permeability increases the compressional phase velocity in the reservoir decreases (Fig. 4). Attenuation effects can also be seen in the reflections corresponding to the bottom of the reservoir as well as in the additional interface included below the sandstone located at ∼0.6 s. Note that such effects are stronger for permeabilities in the vicinity of ∼3.7 and ∼0.4 D for $S_g = 0.1$ and 0.5, respectively. These effects can be inspected in more detail in Fig. 15, where we show the traces corresponding to $\kappa = 0.01$, 3.7 and 10 D for $S_g = 0.1$ and those for $\kappa = 0.01$, 0.4 and 10 D for $S_g = 0.5$. As expected, we observe that the maximum wave deformations occur for $\kappa = 3.7$ and 0.4 D, respectively, since, in agreement with Fig. 4, attenuation and velocity dispersion effects are maximum at those permeability values.

We also performed a corresponding analysis for the case of sandstone 2. Fig. 16 shows the traces corresponding to $\kappa = 0.01$, 1.62 and 10 D for $S_g = 0.1$ and those for $\kappa = 0.01$, 0.17 and 10 D for $S_g = 0.5$. The intermediate permeability values chosen in these experiments correspond to the locations of the peaks of the inverse quality factor as function of permeability for the sandstone 2 and the corresponding gas saturation value for a frequency of 30 Hz. In agreement with Fig. 9, we observe that seismic data do not show an as significant dependence on permeability as in the previous case, since attenuation and velocity dispersion effects are much less significant for this formation. In particular, and in agreement

with Fig. 9, we do not see any variation of the reflectivity associated with the top of the reservoir as the permeability changes. However, we do see a significant variation of the amplitude of the reflection associated with the bottom of the reservoir as well as a slight pushdown, which are due to attenuation and velocity dispersion effects, respectively. As expected, we do indeed see that in both cases the magnitude of the reflectivity is at a minimum for the corresponding intermediate permeability value, since in this case attenuation effects are at a maximum for the dominant source frequency.

5 CONCLUSIONS

In the context of wave-induced fluid flow, we have explored the effects of permeability on the seismic response of sandstone reservoirs characterized by patchy gas–water saturations. Considering various levels of gas saturation as well as a wide range of geometries and sizes of the patches, we performed an exhaustive analysis of the attenuation and velocity dispersion characteristics of seismic body waves as a function of permeability. Our results indicate that wave-induced fluid flow effects may indeed be very significant for a wide range of common and pertinent reservoir conditions and particularly so in the case of soft and porous materials and relatively low levels of overall gas saturation. We also examined the role of Johnson parameters on the attenuation and velocity dispersion behaviour and determined the ranges where they produce, for some range of permeability values included in the interval 0.01–10 D, significant attenuation and velocity dispersion effects in the
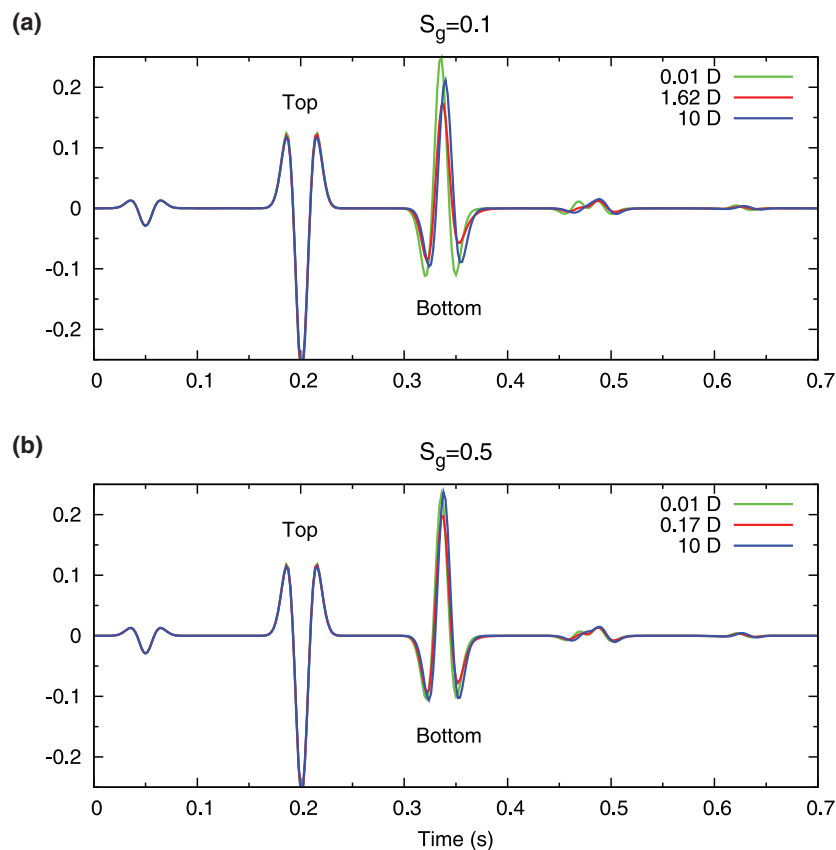

Figure 16. Normal-incidence seismic response of a gas reservoir of the type shown in Fig. 14 for three different permeability values and gas saturations of (a) $S_g = 0.1$ and (b) 0.5. The dry frame properties of the reservoir rock correspond to those of sandstone 2 (Table 1).

frequency range typical of seismic exploration data. In the particular case of spherical gas pockets, we found that for certain permeabilities in this range relatively strong effects arise for patches having diameters ranging from a few centimetres to a few metres. We also observed that for a given frequency within the typical bandwidth of exploration seismic data, the equivalent inverse quality factor as a function of permeability shows a peak, while the phase velocity continuously decreases from the high-frequency limit to the low-frequency limit with increasing permeability.

In a subsequent step, we then explored the corresponding implications for surface-based seismic reflection data by simulating traces of compressional and shear waves reflected from the top of gas reservoirs for various permeability values as well as for a wide range of overall gas saturation levels, patch sizes, and patch geometries. We considered both a soft and porous as well as a harder and less porous sandstone reservoir capped by an elastic shale with a stiffness lying between those of the two reservoir formations. While the reflected shear waves showed negligible sensitivity to permeability, we observed that for soft and porous reservoirs and low gas saturations there is a significant permeability dependence of the compressional seismic response for a wide range of realistic conditions. In the case of the harder and less porous sandstone reservoirs, the normal-incidence response turned out to be insensitive to permeability, while the non-normal-incidence response showed a pronounced sensitivity to permeability, again especially so for low levels of overall gas saturation. We also observed that the reflectivity increases with permeability in the case of gas reservoirs that are softer than their caprock, while the opposite behaviour prevails for reservoirs that are harder than their caprock. Finally, we performed numerical simulations of normal-incidence seismic wave propagation to study the permeability-dependent attenuation and velocity dispersion effects experienced by seismic waves reflected from both the top and the bottom of gas reservoirs. For soft and porous reservoirs and low gas saturation levels, we observed a very significant dependence of the reflection seismic signature on permeability, both in terms of the amplitudes as well as with regard to the two-way traveltime of the reflection from the bottom of the reservoir, whereas for harder and less porous reservoirs the corresponding effects are weak or absent.

The results of this study therefore suggest that in the presence of soft formations and low gas saturation levels, surface-based seismic reflection data may be quite sensitive to the permeability of gas reservoirs, even at normal incidence. For harder and less porous formations this information is contained in the non-normal-incidence reflectivity, which in turn points to the potential of AVA analyses for the hydraulic characterization of these environments.

ACKNOWLEDGMENTS

REFERENCES

Biot, M., 1956a. Theory of propagation of elastic waves in a fluid saturated porous solid. II. Higher frequency range, *J. acoust. Soc. Am,* **28,** 179–191.

Biot, M., 1956b. Theory of propagation of elastic waves in a fluid saturated porous solid. I. Low frequency range, *J. acoust. Soc. Am.,* **28,** 168–178.

Butler, J., 2005. Hydrological methods for estimation of spatial variations in hydraulic conductivity, in *Hydrogeophysics,* pp. 23–58, eds Rubin, Y. & Hubbard, S., Springer, Amsterdam.

Carcione, J., 2007. *Wave Fields in Real Media: Wave Propagation in Anisotropic, Anelastic, Porous and Electromagnetic Media,* Elsevier, Amsterdam.

Carcione, J. & Picotti, S., 2006. P-wave seismic attenuation by slow-wave diffusion: effects of inhomogeneous rock properties, *Geophysics,* **71,** O1–O8.

De Barros, L. & Dietrich, M., 2008. Perturbation of the seismic reflectivity of a fluid-saturated depth-dependent poroelastic medium, *J. acoust. Soc. Am.,* **123,** 1409–1420.

De Barros, L., Dietrich, M. & Valette, B., 2010. Full waveform inversion of seismic waves reflected in a stratified porous medium, *Geophys. J. Int.,* **182,** 1543–1556.

Dutta, N. & Odé, H., 1979. Attenuation and dispersion of compressional waves in fluid-filled porous rocks with partial saturation (White model)—part I: Biot theory, *Geophysics,* **44,** 1777–1788.

Dvorkin, J., Mavko, G. & Nur, A., 1995. Squirt flow in fully saturated rocks, *Geophysics,* **60,** 97–107.

Ellis, D. & Singer, J., 2008. *Well Logging for Earth Scientists,* Springer, Dordrecht.

Goloshubin, G., Silin, D., Vingalov, V., Takkand, G. & Latfullin, M., 2008. Reservoir permeability from seismic attribute analysis, *Leading Edge,* **27,** 376–381.

Gurevich, B. & Lopatnikov, S., 1995. Velocity and attenuation of elastic waves in finely layered porous rocks, *Geophys. J. Int.,* **121,** 933–947.

Hill, R., 1964. Theory of mechanical properties of fiber-strengthened materials, *J. Mech. Phys. Solids,* **11,** 357–372.

Hubbard, S. & Rubin, Y., 2005. Introduction to hydrogeophysics, in *Hydrogeophysics,* eds. Rubin, Y. & Hubbard, S., Springer, Amsterdam.

Johnson, D., 2001. Theory of frequency dependent acoustics in patchy-saturated porous media, *J. acoust. Soc. Am.,* **110,** 682–694.

Kozlov, E., 2007. Seismic signatures of a permeable, dual-porosity layer, *Geophysics,* **72,** SM281–SM291.

Krief, M., Garat, J., Stellingwerff, J. & Ventre, J., 1990. A petrophysical interpretation using the velocities of P and S waves (full waveform inversion), *Log Analyst,* **31,** 355–369.

Liu, L., Cao, S. & Wang, L., 2011. Poroelastic analysis of frequency-dependent amplitude-versus-offset variations, *Geophysics,* **76,** C31–C40.

Masson, Y. & Pride, S., 2011. Seismic attenuation due to patchy saturation, *J. geophys. Res.,* **116,** B03206, doi:10.1029/2010JB007983.

Mavko, G., Mukerji, T. & Dvorkin, J., 2009. *The Rock Physics Handbook: Tools for Seismic Analysis of Porous Media,* 2nd edn, Cambridge University Press, New York, NY.

Morency, C., Luo, Y. & Tromp, J., 2009. Finite-frequency kernels for wave propagation in porous media based upon adjoint methods, *Geophys. J. Int.,* **179,** 1148–1168.

Müller, T. & Gurevich, B., 2005. Wave-induced fluid flow in random porous media: attenuation and dispersion of elastic waves, *J. acoust. Soc. Am.,* **117,** 2732–2741.

Müller, T., Lambert, G. & Gurevich, B., 2007. Dynamic permeability of porous rocks and its seismic signatures, *Geophysics,* **72,** E149–E158.

Picotti, S., Carcione, J., Rubino, J., Santos, J. & Cavallini, F., 2010. A viscoelastic representation of wave attenuation in porous media, *Comput. Geosci.,* **36,** 44–53.

Pride, S., 2005. Relationships between seismic and hydrological properties, in *Hydrogeophysics,* pp. 253–290, eds Rubin, Y. & Hubbard, S., Springer, Amsterdam.

Pride, S. *et al.*, 2003. Permeability dependence of seismic amplitudes, *Leading Edge,* **22,** 518–525.

Pride, S., Berryman, J. & Harris, J., 2004. Seismic attenuation due to wave-induced flow, *J. geophys. Res.,* **109,** B01201, doi:10.1029/2003JB002639

Quintal, B., Schmalholz, S. & Podladchikov, Y., 2009. Low-frequency reflections from a thin layer with high attenuation caused by interlayer flow, *Geophysics,* **74,** N15–N23.

Ren, H., Goloshubin, G. & Hilterman, F., 2009. Poroelastic analysis of permeability effects in thinly layered porous media, *Geophysics,* **74,** N49–N54.

Rubino, J. & Velis, D., 2011. Seismic characterization of thin beds containing patchy carbon dioxide–brine distributions: a study based on numerical simulations, *Geophysics,* **76,** R57–R67.

Rubino, J., Santos, J., Picotti, S. & Carcione, J., 2007. Simulation of up-scaling effects due to wave-induced fluid flow in Biot media using the finite-element method, *J. appl. Geophys.,* **62,** 193–203.

Rubino, J., Ravazzoli, C. & Santos, J., 2009. Equivalent viscoelastic solids for heterogeneous fluid-saturated porous rocks, *Geophysics,* **74,** N1–N13.

Rubino, J., Velis, D. & Sacchi, M., 2011. Numerical analysis of wave-induced fluid flow effects on seismic data: application to monitoring of CO₂ storage at the Sleipner field, *J. geophys. Res.,* **116,** B03306, doi:10.1029/2010JB007997.

Shapiro, S. & Müller, T., 1999. Seismic signatures of permeability in heterogeneous porous media, *Geophysics,* **64,** 99–103.

Tang, X. & Cheng, C., 1996. Fast inversion of formation permeability from Stoneley wave logs using a simplified Biot-Rosenbaum model, *Geophysics,* **61,** 639–645.

Tang, X. & Cheng, C., 2004. *Quantitative Borehole Acoustic Methods,* Elsevier, Amsterdam.

White, J., 1975. Computed seismic speeds and attenuation in rocks with partial gas saturation, *Geophysics,* **40,** 224–232.

White, J., Mikhaylova, N. & Lyakhovitskiy, F., 1975. Low-frequency seismic waves in fluid-saturated layered rocks, *Izvestija Acad. Sci. USSR, Phys. Solid Earth,* **10,** 654–659.

Wood, A., 1955. *A Textbook of Sound,* MacMillan Publishing Company, New York, NY.

APPENDIX A: JOHNSON PARAMETERS

Johnson (2001) developed a theory of the dynamic bulk modulus $\tilde{K}(\omega)$ to describe the crossover from K_{GW} in the low-frequency limit to K_{GH} in the high-frequency limit. To do so, he considered the simplest expression that ensured causality of the solution

$$\tilde{K}(\omega) = K_{GH} - \frac{K_{GH} - K_{GW}}{1 - \zeta + \zeta\sqrt{1 + j\omega\tau/\zeta^2}}, \tag{A1}$$

where ζ can be written in terms of the physical properties of the dry rock and fluid phases as well as the two 'geometrical' parameters S/V and T (Johnson 2001):

$$\zeta = \frac{K_{GH} - K_{GW}}{2K_{GW}}\left(\frac{\tau}{T}\right), \tag{A2}$$

$$\tau = \left(\frac{K_{GH} - K_{GW}}{K_{GH}G}\right)^2, \tag{A3}$$

$$G = \left[\frac{(Z_w + Q_w)M_c(K_g) - (Z_g + Q_g)M_c(K_w)}{\phi S_g K_G(K_g)M_c(K_w) + \phi S_w K_G(K_w)M_c(K_g)}\right]^2 \frac{S}{V}\sqrt{D^*}, \tag{A4}$$

$$Z_i = K_{av}(K_i)\phi^2, \quad i = g, w \tag{A5}$$

$$Q_i = \phi K_{av}(K_i)(\alpha - \phi), \quad i = g, w \text{ and} \tag{A6}$$

$$D^* = \left(\frac{\kappa K_{GH}}{\eta_g\sqrt{D_g} + \eta_w\sqrt{D_w}}\right)^2. \tag{A7}$$

D_i (i = g, w) is the corresponding diffusivity, computed according to eq. (2). The parameter S/V is the specific surface area

of the patches, while the parameter T depends on the geometry of the patches and has relatively simple expressions only in the case of very rudimentary geometries, such as in the case of White's spherical and layered models (White 1975; White *et al.* 1975).

For the case of concentric spherical geometries, as defined by a region g corresponding to an inner gas sphere of radius R_g surrounded by a water region w of outer radius R_w, it is straightforward to show that

$$\frac{S}{V} = 3\frac{R_g^2}{R_w^3}. \tag{A8}$$

T then assumes the following closed form (Johnson 2001)

$$T = \frac{1}{\kappa}\frac{K_{GW}\phi^2}{30R_w^3}\Big\{\big[3\eta_w g_w^2 + 5(\eta_g - \eta_w)g_g g_w - 3\eta_g g_g^2\big]R_g^5$$
$$- 15\eta_w g_w(g_w - g_g)R_g^3 R_w^2$$
$$+ 5g_w[3\eta_w g_w - (2\eta_w + \eta_g)g_g]R_g^2 R_w^3 - 3\eta_w g_w^2 R_w^5\Big\}, \tag{A9}$$

where

$$g_i = \frac{(1 - K_m/K_s)(1/K_R - 1/K_i)}{1 - K_m/K_s - \phi K_m/K_s + \phi K_m/K_R} \quad \text{with} \quad i = g, w. \tag{A10}$$

In the case of the periodic layering, where g and w denote layers of thickness $2L_g$ and $2L_w$, respectively, it can be easily shown that

$$\frac{S}{V} = \frac{1}{L_g + L_w}, \tag{A11}$$

while

$$T = -\frac{1}{\kappa}\frac{K_{GW}\phi^2}{6(L_g + L_w)}\left(\eta_g g_g^2 L_g^3 + 3\eta_g g_g g_w L_g^2 L_w\right.$$
$$\left. + 3\eta_w g_g g_w L_g L_w^2 + \eta_w g_w^2 L_w^3\right). \tag{A12}$$

More generally, the parameter $T_0 = \kappa T$ is independent of the permeability, and, for convenience, we therefore use this parameter in our analysis.

APPENDIX B: SEISMIC RESPONSE AT A PLANE INTERFACE

Let us consider a compressional harmonic plane wave of frequency ω and unit amplitude propagating in the plane (x, z) and arriving at a plane interface at $z = 0$ with an incidence angle θ. The particle displacements in the upper half-space are caused by the contributions of the incident wave and the reflected compressional and shear perturbations, while in the lower half-space they are given by the superposition of the particle displacements generated by the transmitted compressional and shear waves.

To represent the different contributions we use scalar and vector potentials associated with compressional and shear perturbations, respectively. The scalar potentials associated with the compressional perturbations in the upper and lower half-spaces can be written as

$$\gamma_1 = e^{j(\omega t - k_{x_1}^P x - k_{z_1}^P z)} + R_p(\omega)e^{j(\omega t - k_{x_1}^P x + k_{z_1}^P z)}, \tag{B1}$$

$$\gamma_2 = T_p(\omega)e^{j(\omega t - k_{x_2}^P x - k_{z_2}^P z)}, \tag{B2}$$

where $R_p(\omega)$ and $T_p(\omega)$ are the compressional reflection and transmission coefficients, respectively. The vectors $\mathbf{k}_i^P = (k_{x_i}^P, \pm k_{z_i}^P)$,

with $i = 1, 2$, are the wave vectors associated with the compressional perturbations in the upper ($i = 1$) and lower ($i = 2$) half-spaces and their moduli are given by

$$k_i^p = \omega \sqrt{\frac{\rho_i}{\lambda_i + 2\mu_i}}, \tag{B3}$$

where ρ_i is the density and λ_i and μ_i are the Lamé constant and the shear modulus of the corresponding medium.

The vector potentials associated with the shear perturbations in the two half-spaces are given by

$$\psi_1 = R_s(\omega) e^{j(\omega t - k_{x_1}^s x + k_{z_1}^s z)} \check{e}_2, \tag{B4}$$

$$\psi_2 = T_s(\omega) e^{j(\omega t - k_{x_2}^s x - k_{z_2}^s z)} \check{e}_2, \tag{B5}$$

where $R_s(\omega)$ and $T_s(\omega)$ are the shear reflection and transmission coefficients, respectively, and $\check{e}_2$ denotes the unit vector along the y-axis. In addition, $\mathbf{k}_i^s = (k_{x_i}^s, \pm k_{z_i}^s)$, with $i = 1, 2$, are the wave vectors associated with the shear perturbations in the upper ($i = 1$) and lower ($i = 2$) half-spaces, with their moduli given by $k_i^s = \omega \sqrt{\frac{\rho_i}{\mu_i}}$.

The particle displacements in the upper ($i = 1$) and lower ($i = 2$) half-spaces are given by

$$\mathbf{u}^i = \nabla \gamma_i + \nabla \times \psi_i. \tag{B6}$$

Substituting eqs (B1)–(B5) into eq. (B6), and requiring the continuity of the horizontal component of the particle displacement at the interface, it is straightforward to show that

$$k_{x_1}^p = k_{x_2}^p = k_{x_1}^s = k_{x_2}^s, \tag{B7}$$

which is indeed Snell's law. Taking into account that $k_{x_1}^p = k_1^p \sin\theta$ and using the relation (B7) we find that

$$k_{z_i}^\beta = \left[\left(k_i^\beta \right)^2 - \left(k_1^p \sin\theta \right)^2 \right]^{1/2} \quad \text{with} \quad \beta = p, s \quad \text{and} \quad i = 1, 2. \tag{B8}$$

Next, using the elastic properties of each half-space, we relate the displacement vectors to the stress tensors through Hook's law. As usual, we require the continuity of the displacements and the normal and shear stresses across the interface. This leads to a 4×4 linear system of equations, where the unknowns are the four potential amplitudes, which, in turn, let us obtain the Fourier transforms of the displacements related to the reflected compressional and shear waves.

To account for the effective viscoelastic behaviour of a porous medium characterized by patchy saturation, the corresponding wavenumbers associated with the compressional wave and the Lamé constants must be complex-valued and frequency-dependent. To this end, we consider a compressional wave propagating through such viscoelastic solid and relate the phase velocity and inverse quality factor with the wavenumber in the form

$$V_p(\omega) = \frac{\omega}{\Re(k_i^p)}, \tag{B9}$$

$$\frac{1}{Q(\omega)} = -2 \frac{\Im(k_i^p)}{\Re(k_i^p)}, \tag{B10}$$

where $V_p(\omega)$ and $Q(\omega)$ are given by eqs (14) and (15).

The corresponding wavenumber is then given by

$$k_i^p = \frac{\omega}{V_p(\omega)} \left[1 - \frac{j}{2Q(\omega)} \right], \quad i = 1, 2. \tag{B11}$$

In addition, we obtain from eq. (B3)

$$\lambda_i = \rho_i \frac{\omega^2}{(k_i^p)^2} - 2\mu_i, \quad i = 1, 2. \tag{B12}$$